THE *HERSCHEL* EXPLOITATION OF LOCAL GALAXY ANDROMEDA (HELGA). II. DUST AND GAS IN ANDROMEDA[*]

M. W. L. Smith[1], S. A. Eales[1], H. L. Gomez[1], J. Roman-Duval[2], J. Fritz[3], R. Braun[4], M. Baes[3], G. J. Bendo[5],
J. A. D. L. Blommaert[6], M. Boquien[7], A. Boselli[7], D. L. Clements[8], A. R. Cooray[9], L. Cortese[10], I. de Looze[3],
G. P. Ford[1], W. K. Gear[1], G. Gentile[3], K. D. Gordon[2,3], J. Kirk[1], V. Lebouteiller[11], S. Madden[11], E. Mentuch[12],
B. O'Halloran[8], M. J. Page[13], B. Schulz[14], L. Spinoglio[15], J. Verstappen[3], C. D. Wilson[16], and D. A. Thilker[17]

[1] School of Physics & Astronomy, Cardiff University, The Parade, Cardiff CF24 3AA, UK; Matthew.Smith@astro.cf.ac.uk
[2] Space Telescope Science Institute, 3700 San Martin Drive, Baltimore, MD 21218, USA
[3] Sterrenkundig Observatorium, Universiteit Gent, Krijgslaan 281 S9, B-9000 Gent, Belgium
[4] CSIRO Astronomy and Space Science, P.O. Box 76, Epping, NSW 1710, Australia
[5] UK ALMA Regional Centre Node, Jodrell Bank Centre for Astrophysics, School of Physics and Astronomy,
University of Manchester, Oxford Road, Manchester M13 9PL, UK
[6] Instituut voor Sterrenkunde, K.U. Leuven, Celestijnenlaan 200D, B-3001 Leuven, Belgium
[7] Laboratoire d'Astrophysique de Marseille-LAM, Universit d'Aix-Marseille & CNRS, UMR7326, 38 Rue F. Joliot-Curie, F-13388, Marseille Cedex 13, France
[8] Astrophysics Group, Imperial College, Blackett Laboratory, Prince Consort Road, London SW7 2AZ, UK
[9] Center for Cosmology and the Department of Physics & Astronomy, University of California, Irvine, CA 92697, USA
[10] European Southern Observatory, Karl Schwarschild Str. 2, D-85748, Garching bei Muenchen, Germany
[11] CEA, Laboratoire AIM, Irfu/SAp, Orme des Merisiers, F-91191, Gif-sur-Yvette, France
[12] Astronomy Department, University of Texas at Austin, Austin, TX 78712, USA
[13] Mullard Space Science Laboratory, University College London, Holmbury St. Mary, Dorking, Surrey RH5 6NT, UK
[14] Infrared Processing and Analysis Center, MS 100-22, California Institute of Technology, JPL, Pasadena, CA 91125, USA
[15] Istituto di Fisica dello Spazio Interplanetario, INAF, Via del Fosso del Cavaliere 100, I-00133 Roma, Italy
[16] Department of Physics & Astronomy, McMaster University, Hamilton, ON, L8S 4M1, Canada
[17] Department of Physics & Astronomy, Johns Hopkins University, 3400 N. Charles St., Baltimore, MD 21218, USA

ABSTRACT

We present an analysis of the dust and gas in Andromeda, using *Herschel* images sampling the entire far-infrared peak. We fit a modified-blackbody model to ∼4000 quasi-independent pixels with spatial resolution of ∼140 pc and find that a variable dust-emissivity index (β) is required to fit the data. We find no significant long-wavelength excess above this model, suggesting there is no cold dust component. We show that the gas-to-dust ratio varies radially, increasing from ∼20 in the center to ∼70 in the star-forming ring at 10 kpc, consistent with the metallicity gradient. In the 10 kpc ring the average β is ∼1.9, in good agreement with values determined for the Milky Way (MW). However, in contrast to the MW, we find significant radial variations in β, which increases from 1.9 at 10 kpc to ∼2.5 at a radius of 3.1 kpc and then decreases to 1.7 in the center. The dust temperature is fairly constant in the 10 kpc ring (ranging from 17 to 20 K), but increases strongly in the bulge to ∼30 K. Within 3.1 kpc we find the dust temperature is highly correlated with the 3.6 μm flux, suggesting the general stellar population in the bulge is the dominant source of dust heating there. At larger radii, there is a weak correlation between the star formation rate and dust temperature. We find no evidence for "dark gas" in M31 in contrast to recent results for the MW. Finally, we obtained an estimate of the CO X-factor by minimizing the dispersion in the gas-to-dust ratio, obtaining a value of $(1.9 \pm 0.4) \times 10^{20}$ cm^{-2} [K km s^{-1}]$^{-1}$.

Key words: galaxies: evolution – galaxies: individual (M31) – galaxies: ISM – Local Group

Online-only material: color figures

1. INTRODUCTION

Astronomy at long infrared wavelengths (20–1000 μm) is a relatively young field due to the need for space missions to avoid the absorption of the atmosphere in this waveband. This waveband, however, is vital for astronomical studies as this is where dust in the interstellar medium (ISM) radiates. This is important for studies of galaxy evolution as star formation regions tend to be dusty, and therefore the use of UV and optical measurements to trace the star formation rate (SFR) can lead to it being underestimated (see Kennicutt 1998; Blain et al. 1999; Calzetti 2001; Papovich & Bell 2002; Calzetti et al. 2010). Calibrating the relationship between infrared emission and SFR has been difficult due to uncertainties from the contribution of

the general stellar population to heating the dust, the fact that not all optical/UV emission is absorbed, and uncertainties in the properties of the dust. The dust emission is affected by the composition of the dust and the proportion of non-equilibrium to equilibrium heating. Studies with previous space missions *IRAS*, *ISO*, *Spitzer*, and *AKARI* tried to address these questions (e.g., Walterbos & Greenawalt 1996; Boselli et al. 2004; Calzetti et al. 2010; Buat et al. 2011). However, as they were limited to wavelengths less than 160 μm, they were not sensitive to the cold dust (⩽15 K) and missed up to 50% of the dust mass in galaxies.

The continuum emission from the dust has been proposed as a potential method of measuring the total mass of the ISM (Hildebrand 1983; Guelin et al. 1993; Eales et al. 2010, 2012); traditionally the amount of gas has been measured using H I and CO surveys, but due to sensitivity and resolution issues this method is limited to low redshift and small numbers of

galaxies. Smith et al. (2012) found that for early-type galaxies (E/S0) the ISM was detected for 50% of objects through its dust emission but only 22% through its CO emission. In addition, the conversion of the CO tracer to molecular gas mass is highly uncertain and is believed to vary with metallicity (see Wilson 1995; Boselli et al. 2002; Strong et al. 2004; Israel 2005; Narayanan et al. 2012). This is a topical area as recent studies using the *Planck* all-sky survey and *IRAS* maps have made an estimate of the amount of "dark gas" (Planck Collaboration 2011a) in the Milky Way (MW). The "dark gas" is thought to be molecular gas which is traced by dust, but not detected with the standard CO method. Previous works have also suggested the presence of "dark gas" by using γ-ray emission from cosmic-ray interactions with clouds of gas (Grenier et al. 2005; Abdo et al. 2010) and by the kinematics of recycled dwarf galaxies (Bournaud et al. 2007).

Herschel is one of the European Space Agency's flagship observatories and observes in the far-infrared (FIR) in the range of 55–671 μm (see Pilbratt et al. 2010). Due to the large space mirror and cryogenic instruments, it has a high sensitivity and unprecedented angular resolution at these wavelengths. *Herschel* has the ability to target both large numbers of galaxies and map large areas of sky. It has two photometric instruments: PACS (Poglitsch et al. 2010) which can observe in three broad bands around 70, 100, and 160 μm (70 and 100 μm cannot be used simultaneously) and SPIRE (Griffin et al. 2010) which observes simultaneously in filter bands centered at 250, 350, and 500 μm. SPIRE provides flux measurements on the longer wavelength side of the FIR dust peak ($\sim$160 μm), allowing us to obtain a full census of dust in nearby galaxies (e.g., Dunne et al. 2011).

Andromeda (M31) and the MW are the only two large spirals in the Local Group. Studies of Andromeda therefore provide the best comparison to observations of our own Galaxy with the advantage that we get a "global" picture, whereas investigations of the MW are limited by our location within the Galaxy. The total size of M31 and the scalelength of its disk are both approximately twice those of the MW (see Yin et al. 2009, and references therein). However, the SFR of the MW is $\sim$3–6 $M_\odot$ yr^{-1} (Boissier & Prantzos 1999) compared to only $\sim$0.3–1.0 in M31 (Barmby et al. 2006; Williams 2003; G. P. Ford et al., in preparation), despite similar amounts of gas present (Yin et al. 2009). For this reason, M31 is often labeled as "quiescent." The dust emission from M31 is dominated by a dusty star-forming ring at a radius of 10 kpc and was first observed in the infrared by *IRAS* (Habing et al. 1984).

Many projects to map the ISM in M31 have been undertaken using observations in the mid-infrared (MIR) with *Spitzer* (Barmby et al. 2006), in the FIR with *Spitzer* (Gordon et al. 2006), in the H I atomic line (Thilker et al. 2004; Braun et al. 2009; Chemin et al. 2009), and in the CO($J = 1$–0) line (Nieten et al. 2006). Studies of the gas kinematics and dust emission show that M31 has a complicated structure (e.g., Chemin et al. 2009; Gordon et al. 2006); Block et al. (2006) attribute many of the features observed to density waves from a possible head-on collision with M32. Tabatabaei & Berkhuijsen (2010) investigated the relation between gas, dust, and star formation using FIR *Spitzer* data. Leroy et al. (2011) used *Spitzer* and gas observations to investigate the conversion between CO($J = 1$–0) line flux and molecular hydrogen column density in a sample of nearby galaxies including M31. In their analysis, they found that M31 has the lowest dust temperatures in their sample and therefore would benefit most by including *Herschel* data.

The *Herschel* Exploitation of Local Galaxy Andromeda (HELGA) is a survey covering a $\sim$5°.5 × 2°.5 area centered on M31. We use PACS–SPIRE parallel mode, observing at 100, 160, 250, 350, and 500 μm simultaneously. Further details of the observations can be found in Section 2.1 and in Fritz et al. (2011). HELGA observations have been used in other works to investigate structures in dust and H I at large radii (Fritz et al. 2011), the relationship between gas and star formation (G. P. Ford et al., in preparation), and the structure of M31 and the cloud-mass function (J. Kirk et al., in preparation).

In this paper, we use the *Herschel* data combined with the wealth of ancillary data to investigate the distribution, emission properties, and the processes heating the dust in M31 on spatial scales of $\sim$140 kpc. There have still been relatively few attempts to map the dust within a galaxy; recent studies with *Herschel* include Smith et al. (2010), Boquien et al. (2011), Foyle et al. (2012), Bendo et al. (2012), and Mentuch et al. (2012), but they are often limited to small numbers of independent pixels. The advantage of M31 over these other studies is the close proximity which allows us to investigate the dust at higher spatial scale and with many more independent pixels. We also apply the Planck method for finding "dark gas" (Planck Collaboration 2011a) to M31 and use this method to determine a value of the X-factor—the relationship between the molecular hydrogen column density and the observed CO tracer. In Section 2, we present the data used for this analysis and Section 3 describes our method for fitting the spectral energy distribution (SED) of dust. Section 4 presents our maps of the dust properties, including the distribution of dust surface density, temperature, and spectral index. This section also describes a comparison of the distributions of gas and dust and of the search for an excess emission at long wavelengths. In Section 5, we discuss the dust properties including the composition of the dust and the processes heating the dust. In this section, we also search for "dark gas" and determine the value of the X-factor. The conclusions are presented in Section 6.

2. THE DATA

2.1. Far-infrared Observations

Herschel observations of M31 were taken using both PACS and SPIRE in parallel mode covering an area of $\sim$5°.5 × 2°.5 centered on M31. To observe an area this large, the observations were split into two halves with a cross-scan on each half, which produced data at 100, 160, 250, 350, and 500 μm simultaneously (observation IDs: 1342211294, 1342211309, 1342211319, 1342213207). Full details of the observing strategy and data reduction can be found in Fritz et al. (2011).

The PACS data reduction was performed in two stages. The initial processing up to Level-1 (i.e., to the level where the pointed photometer timelines have been calibrated) is performed in HIPE v8.0 (Ott 2010) using the standard pipeline. To remove low-frequency noise (or drifts) in the arrays, residual glitches, and create the final maps, we use SCANAMORPHOS (v15; Roussel 2011). The final maps have a pixel scale of 2$''$ and 3$''$ and a spatial resolution of 12$''$.5 and 13$''$.3 FWHM at 100 and 160 μm, respectively.

The SPIRE data were processed up to Level-1 with a custom pipeline script adapted from the official pipeline. We apply the latest flux correction factors from the SPIRE Instrument Control Centre to update the maps to the latest calibration product (SPIRE Observer's Manual 2011). For the baseline subtraction
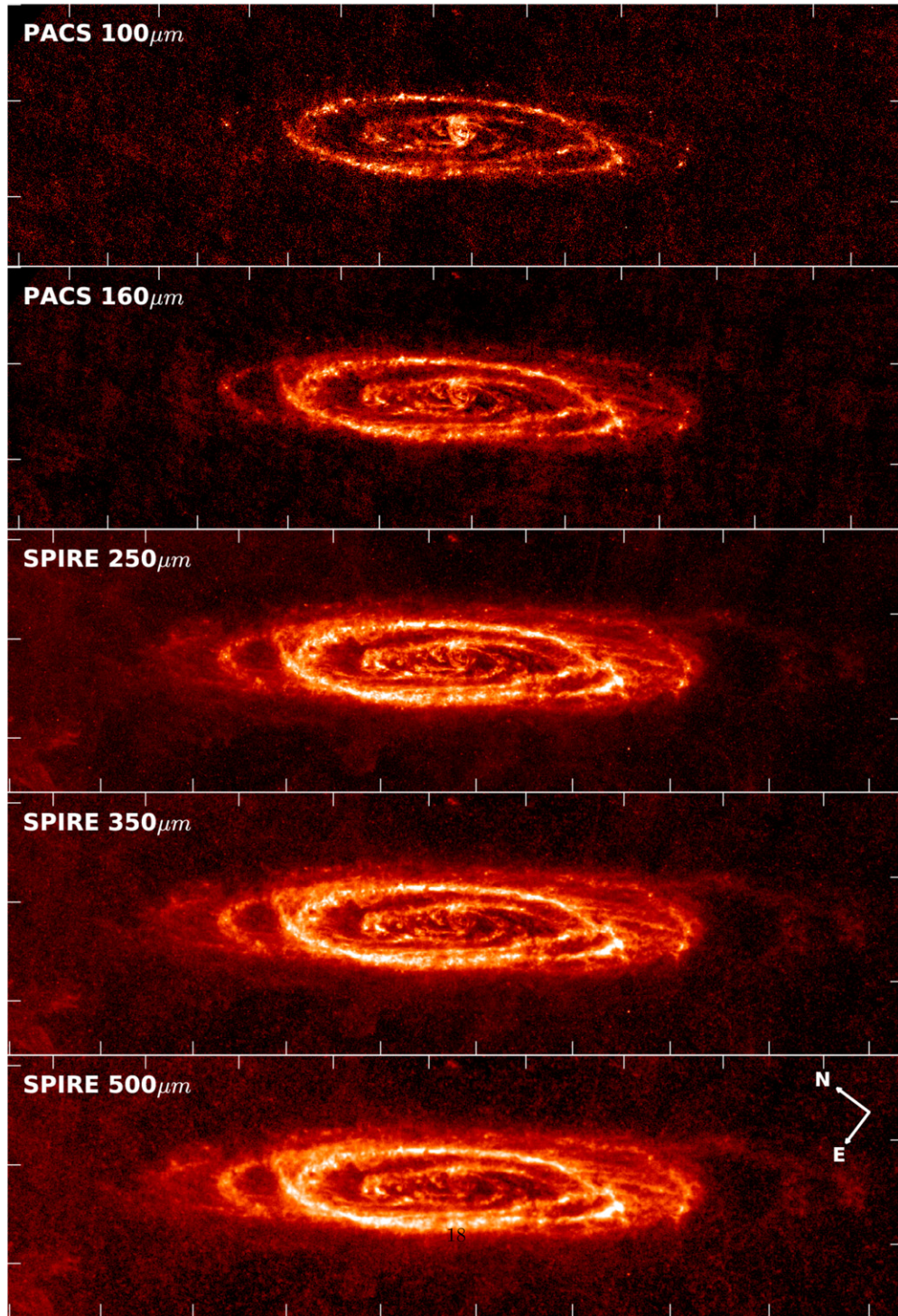
Figure 1. *Herschel* images used in the analysis of this paper. The images have dimensions of approximately $4°\!.5 \times 1°\!.3$, with a tick spacing of $30'$ and centered on $10^h43^m02^s$, $+41°17'42''$. These images are all at their original resolution.

(A color version of this figure is available in the online journal.)

we use a custom method called BRIGADE (M. W. L. Smith et al., in preparation) which uses an alternative technique for correcting temperature drifts. The final maps were created using the naive mapper with pixel sizes of $6''$, $8''$, and $12''$ with spatial resolution of $18''\!.2$, $24''\!.5$, $36''\!.0$ FWHM for the 250, 350, and 500 μm maps, respectively. All *Herschel* images are shown in Figure 1.

In addition to the *Herschel* data, we make use of the 70 μm *Spitzer*/MIPS (Rieke et al. 2004) map published in Gordon et al. (2006). This observation covers a region of M31 approximately $3° \times 1°$ in size and has an exposure time of $\sim$40 s pixel^{-1}. The data were processed using the MIPS Data Analysis Tool version 2.90 (Gordon et al. 2005) and full details of the reduction can be found in Gordon et al. (2006).
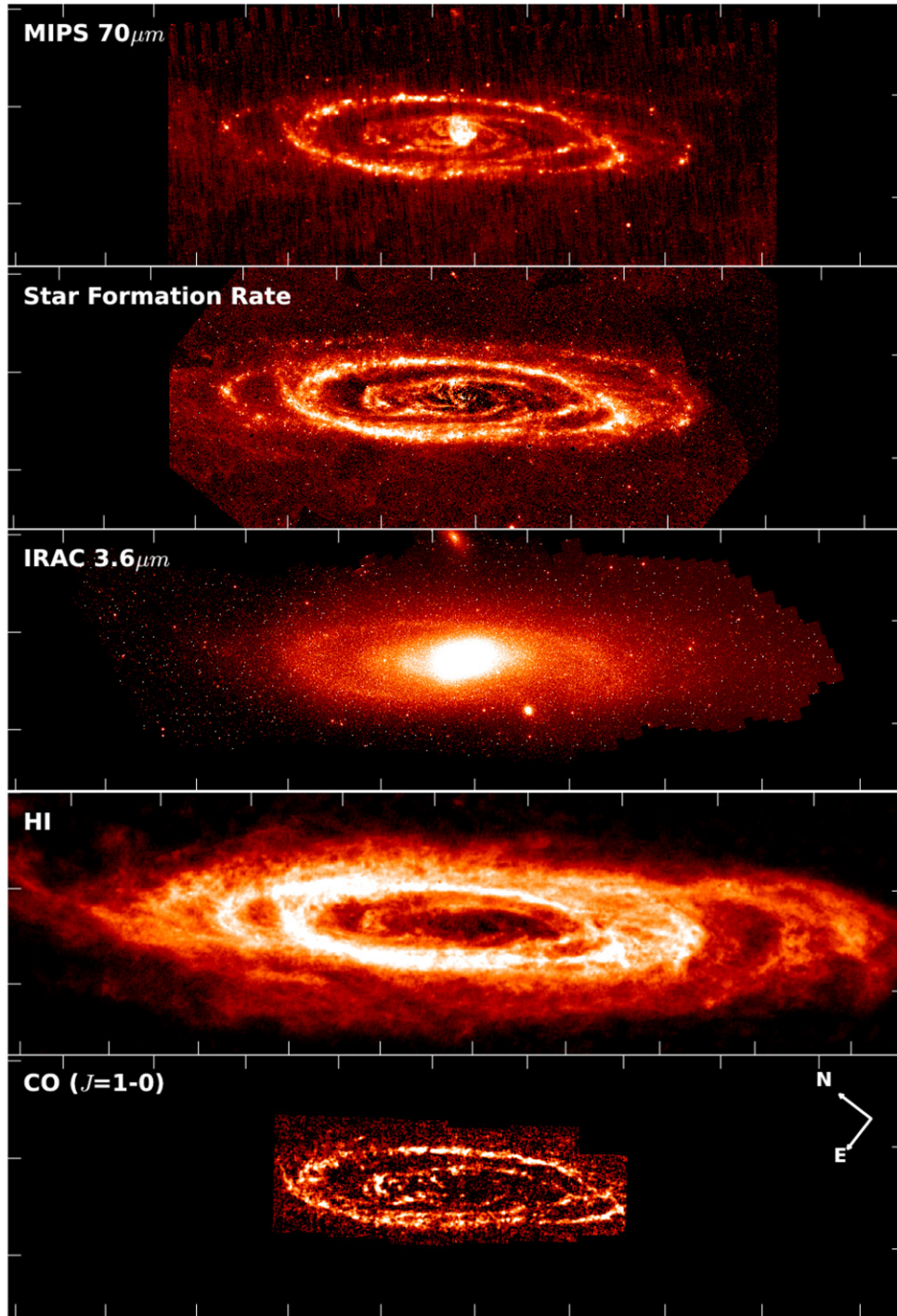
Figure 2. Ancillary images for M31. The scale is the same as for the *Herschel* images presented in Figure 1. From top: *Spitzer*/MIPS 70 μm, the star formation rate (presented in G. P. Ford et al., in preparation), *Spitzer*/IRAC 3.6 μm (presented in Barmby et al. 2006), H I and CO images as in Figure 1. The CO map (used as a tracer of H_2) only covers an area of $2° \times 0°.5$. These images are all at their original resolution.

(A color version of this figure is available in the online journal.)

2.2. Gas Measurements

To investigate the atomic hydrogen in Andromeda we use the H I moment-zero map presented in Braun et al. (2009). The observations were made with the Westerbork Synthesis Radio Telescope covering a region of $\sim 6° \times 3°.5$ with a resolution of $18'' \times 15''$. In this work, we present our results using a map which has not been corrected for opacity effects since this correction is uncertain. For the results which make use of the H I map we also test how our results are affected by using an H I map corrected for self-opacity using the prescription outlined in Braun et al. (2009). The uncorrected H I map has a sensitivity of 4.2×10^{18} cm^{-2}.

For the molecular hydrogen gas content, we use CO($J = 1$–0) observations presented in Nieten et al. (2006) made with the IRAM 30 m telescope. This covers an area of $2° \times 0°.5$ with a sensitivity of $\sim$0.35 K km s^{-1}.

All maps other than the *Herschel* images used for this analysis are shown in Figure 2.

3. THE FIR–SUBMILLIMETER SPECTRAL
ENERGY DISTRIBUTION

To investigate how the dust properties vary across M31, we undertake a pixel-by-pixel dust analysis, using the *Spitzer* 70 μm, *Herschel*/PACS, and SPIRE images. We first convolve the data to the same resolution as the 500 μm map (our largest FWHM) by using a kernel which matches the point-spread function in a particular band to the 500 μm band. This procedure is described in detail in Bendo et al. (2012). The images are then re-binned into 36″ pixels, chosen to be about the same size as the 500 μm beam so that each pixel is approximately independent from each other. For each band we subtract a background value for the whole map, estimated from regions around the galaxy. The uncertainties on the flux in each pixel are found by measuring the standard deviation of the pixels in these background regions and adding this in quadrature with the calibration uncertainty. The flux errors in the majority of pixels are dominated by the calibration uncertainty which we take as 7% for *Spitzer* 70 μm (Gordon et al. 2007), 10% for PACS (see Fritz et al. 2011), and 7% for SPIRE (see Section 3.1 for more details).

3.1. SED Fitting

For each pixel we fit the far-infrared–submillimeter SED with a one-temperature modified-blackbody model described by

$$S_\nu = \frac{\kappa_\nu M_d B(\nu, T_d)}{D^2}, \tag{1}$$

where M_d is the dust mass with dust temperature T_d, $B(\nu, T_d)$ is the Planck function, and D is the distance to the galaxy. κ_ν is the dust absorption coefficient, described by a power law with dust emissivity index β such that $\kappa_\nu \propto \nu^\beta$. We assume a typical value for the ISM of $\kappa_{350\,\mu m} = 0.192\,\mathrm{m}^2\,\mathrm{kg}^{-1}$ (Draine 2003). While the absolute value of κ_ν is uncertain, its value will not affect trends with other parameters as it is a fixed scaling constant. The distance to Andromeda was taken in this work to be $D = 0.785$ Mpc (McConnachie et al. 2005).

We initially used a fixed value of β across the whole galaxy, but we found that with a fixed value it was impossible to adequately fit the SEDs; we therefore let β be a free parameter. To ensure that the simplex fitting routine did not get stuck in a local minimum, we ran the SED fitter in two ways: first with all three parameters (M_d, T_d, β) free to vary; second by fixing the value of β while allowing M_d and T_d to vary and repeating the process for all values of β in the range 0.20–5.90 in 0.01 intervals, selecting the result with the lowest χ^2. Both methods gave consistent results, but we created the final maps of the dust properties by choosing the result with the lowest χ^2 for each pixel.

The SPIRE calibration has an overall systematic uncertainty of 5% due to the uncertainty in the prime calibrator Neptune, and a statistical uncertainty of 2% determined from instrumental reproducibility; the SPIRE Observer's Manual recommends linearly adding these to give an overall uncertainty of 7%. To implement this in practice in our fitting algorithm, we increased the uncorrelated uncertainty to give the same overall uncertainty when the errors are added in quadrature. This is implemented in the SED fitting by using the full covariance matrix in the χ^2 calculation.

We apply our own color correction to the *Herschel* maps by removing the *Herschel* pipeline "K4" parameter and then convolving the SED with the filter transmission in the fitting

process (for SPIRE the filters appropriate for extended sources are used). This method takes full account of all the wavelength-dependant effects associated with PACS and SPIRE. In previous work (Smith et al. 2010), we found that there is a significant contribution from a warmer component of dust at wavelengths ⩽70 μm and so the *Spitzer* flux at 70 μm is treated as an upper limit in the fitting (i.e., if the flux value is higher than the model it does not contribute to χ^2). The omission of the warm component in the fitting process has a negligible effect on the derived dust mass as the cold component dominates the total dust mass. Bendo et al. (2012) suggest that a warmer component could influence the dust emission up to wavelengths of 160 μm; to test this we repeated the SED fitting by treating the *Spitzer* and PACS fluxes as upper limits and found that it made a negligible difference to our results.

To estimate the uncertainties on the results of our fits we use a Monte Carlo technique. For each pixel we create a set of 1000 artificial SEDs, created by taking the original flux densities and adding a random value selected from a normal distribution with a mean of zero and a standard deviation equal to the uncertainty in the measured flux (the correlations between the calibration uncertainties for SPIRE are also included). We estimate the error in the derived parameters for each pixel from the 1000 fits. We find that for each pixel there is an uncertainty of 20% in our estimate of the surface density of the dust, of ±1.4 K in our estimate of the dust temperature, and ±0.31 in our estimate of β.

3.2. Results of the Fits

In producing the final dust mass, temperature, and β images in this work, we only used pixels where the fluxes in all six bands (five *Herschel* and MIPS 70 μm) have a signal-to-noise ratio greater than 5σ. While this potentially causes us to miss the very coldest dust due to weak emission in the shortest wavelength bands, we choose it as a conservative approach to ensure that we have accurate estimates of temperature. In practice it is the 100 μm map, which has the lowest sensitivity, that limits the number of pixels in our selection. Despite this very conservative selection, there are still ∼4000 pixels in our resultant maps. To see if our model is a statistically reasonable fit to the data, we created a histogram of the χ^2 values for all pixels (Figure 3). As the 70 μm flux is used as an upper limit (see Section 3.1) and is usually higher than the best-fit model, it does not usually contribute to χ^2 and therefore we only have 1 degree of freedom (5$_{\mathrm{data\ points}}$ − 3$_{\mathrm{parameters}}$ − 1). The 10% significance level for χ^2 occurs at 2.71, which is shown by the red line in Figure 3. We find 9.8% of our fits have χ^2 above this level showing our model is an adequate representation of the data. We have also checked to see if our radial gradients in temperature, β, and dust surface density are affected by lowering the criteria to include fluxes greater than 3σ and find no significant changes.

Recent results from the Key Insight on Nearby Galaxies: A Far-Infrared Survey with *Herschel* presented in Dale et al. (2012) have suggested that the one-temperature modified-blackbody model underestimates the dust mass compared to the Draine & Li (2007) prescription. They attribute this difference to the contribution of warm dust emitting at shorter wavelengths. For our analysis this does not appear to be the case. First, when we set the PACS fluxes (⩽160 μm) as upper limits there is no significant change in our results. Second, if multiple temperature components were present this would bias our β values to lower values (since each temperature component peaks at a different
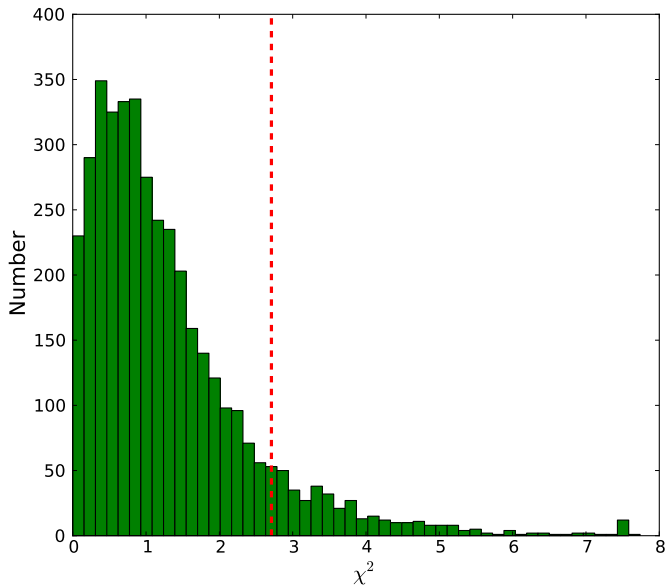
Figure 3. Distribution of χ^2 values from pixels fitted with the modified-blackbody model. The red line represents the 10% significance value for 1 degree of freedom.
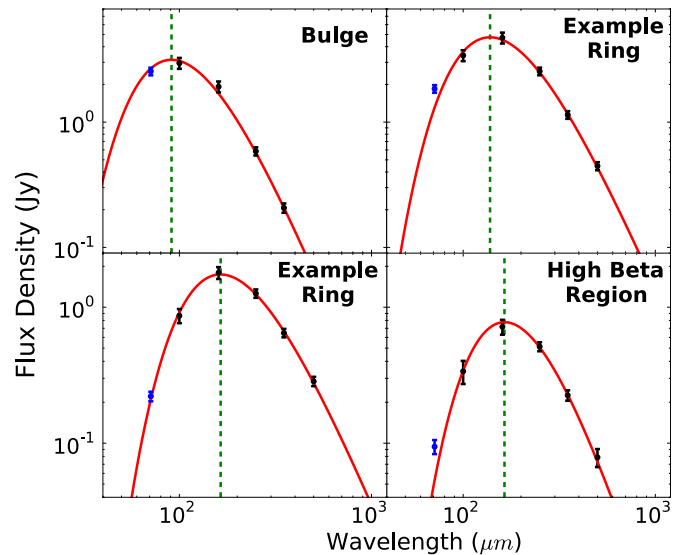
(A color version of this figure is available in the online journal.)

Figure 4. Examples of SED fits for pixels in different regions. The 70 μm point (blue) is used as an upper limit and the peak of distribution is shown by the dashed green line.

(A color version of this figure is available in the online journal.)

wavelength; Shetty et al. 2009b), but we mostly find higher β values than expected (see Section 4). Third the χ^2 analysis suggests the model is consistent with the data. In addition, Mentuch et al. (2012), using a similar analysis, have found in M51 that the dust mass distribution is similar when using the Draine & Li (2007) or the single modified-blackbody prescription.

We applied the same fitting technique as outlined in Section 3.1 to the global flux densities, measured in an elliptical aperture with a semimajor axis of $2°.0$ and semiminor axis of $0°.73$. This produces a total dust mass of $10^{7.86\pm0.09}\,M_\odot$ with a dust temperature of 16.1 ± 1.1 K and $\beta = 1.9 \pm 0.3$. The total dust mass from summing all the pixels in our pixel-by-pixel analysis gives a value $10^{7.46}\,M_\odot$, a factor of ~2.5 lower. This is expected as the fraction of 500 μm flux in the pixels that satisfy our signal-to-noise criterion is approximately half the global value. Combining our global dust mass with gas measurements, we find a global gas-to-dust mass ratio of 72. The global temperature is consistent with these for other spiral galaxies obtained using similar methods (e.g., Davies et al. 2012). The pixel-by-pixel analysis shows a large range of temperatures and β values as discussed in detail in Section 4. Examples of fits for individual pixels are shown in Figure 4.

3.3. Simulations

To help understand the significance of our results and any potential biases or degeneracies in the parameters, we ran a Monte Carlo simulation. Assuming the dust emits as a single-component modified blackbody, we generated synthetic flux values for a range of temperatures and β values, with the same wavelengths as our real data. Noise was then added to the simulated fluxes with a value equal to the errors in the real fluxes (excluding the calibration errors) for 2000 repetitions per T, β combination. The calibration error was not included as it would systematically shift the fluxes for all pixels. We chose an input mass surface density of $0.5\,M_\odot\,\mathrm{pc}^{-2}$ as this roughly corresponds to the values found in the 10 kpc ring.
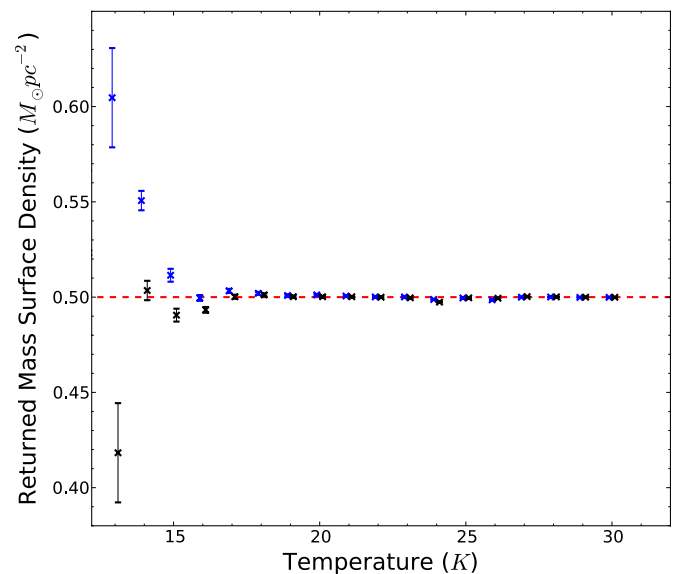

Figure 5. Range of mass surface densities returned from the SED-fitting technique vs. the input temperature for the simulated data in Section 3.3 with $\beta = 2$ modified blackbody. The mean of the returned masses is shown by the blue points and the median is shown by the black points. The input mass surface density of $0.50\,M_\odot\,\mathrm{pc}^{-2}$ is shown by the red dashed line. To avoid overlapping data points the blue have been shifted by -0.1 K and the black by $+0.1$ K.

(A color version of this figure is available in the online journal.)

The quantity that is most important for our work is the dust mass, which from Equation (1) is just a multiplicative term. Figure 5 shows the mean and median mass returned for the 2000 repetitions as the input temperature is varied between 12 and 30 K for a β of 2; the error bars show the error on the mean. Between 15 and 30 K, the mean and median dust mass returned matches within the errors the input dust surface density of $0.50\,M_\odot\,\mathrm{pc}^{-2}$.

At dust temperatures of 15 K and below, there are large errors on the returned mass, which is due to the fluxes at the PACS wavelengths not reaching the required sensitivity to be included
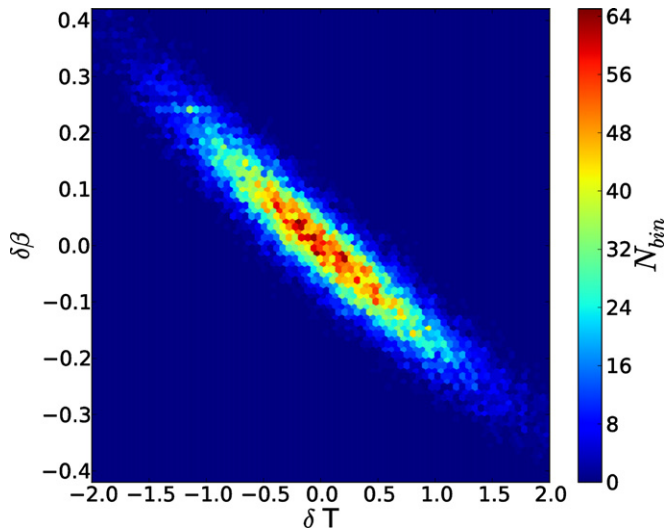
Figure 6. Density plot showing the correlated uncertainties between β and temperature. The uncertainties are taken from the simulated data with $T = 17$ K and $\beta = 1.8$. A clear anti-correlation is observed with the distribution centered on the correct values. To fully populate this graph we increased the simulation to 20,000 repetitions for this β, T combination.

(A color version of this figure is available in the online journal.)

in the fit. For the actual data, we only included pixels in which there is at least a 5σ detection in all bands, which will avoid the wildly incorrect estimates of the dust mass seen in the simulation. To fully estimate the dust mass and temperature of very cold dust ($T < 15$ K), we need flux measurements at $>500\,\mu$m. Nevertheless, the lack of an excess at $500\,\mu$m (Section 4.3) is circumstantial evidence that Andromeda does not contain very cold dust. We investigated if the results in Figure 5 were different for a different choice of β but found no systematic differences.

By plotting the difference in the resultant temperature in each pixel compared to the input model temperature, we find that between 15 K and 25 K, the temperature uncertainty is $\sim$0.6 K. Above 25 K the uncertainty increases, although in the simulation we did not include a $70\,\mu$m point which would likely provide a constraint to our fits if the dust temperature was >25 K. The simulation suggests that for input β between 1.5 and 2.4, the uncertainty in the returned value of β for each pixel is $\sim$0.1. As expected these uncertainties are lower than returned by the Monte Carlo technique in Section 3.1 as we have not included a calibration uncertainty.

A degeneracy is known to exist between temperature and β; Figure 6 shows that if there is an error in one parameter this is anti-correlated with the error in the other parameter. As the distribution is centered on the origin, there is no systematic offset in the returned value of T or β. As there is no systematic offset, the error in the mean values over many pixels will therefore be much smaller than the error for a single pixel.

This simulation is based on the dust emission arising from a one-component modified blackbody. Fitting a one-component modified blackbody to pixels for which there are multiple temperature components would produce a bias toward smaller values of β (Shetty et al. 2009b), although we would hope to detect this by finding high χ^2 values. In Section 5.2, we show that different regions of M31 have different β–T relations and discuss why this is unlikely to be due to multiple temperature components.

To summarize, while there is a β–T degeneracy from the fitting algorithm this does not create any systematic offsets in the value returned. If the dust temperature falls below 15 K we are unable to constrain the SED due to the lack of data points beyond $500\,\mu$m.

4. RESULTS

4.1. Spatial Distribution of Dust Mass, Temperature, and Emissivity Index

By fitting SEDs to every pixel, we have created maps of dust surface density, temperature, β, and gas-to-dust ratio which are shown in Figure 7 (for details on how the gas surface density is calculated see Section 4.2). The dust surface density distribution, unsurprisingly, is more similar to the maps of gas and SFR than to the $3.6\,\mu$m image (see Figures 1 and 2), which traces the stellar mass distribution.

The β and temperature maps show significant radial variations. Figure 8 shows how the dust column density, temperature, and β vary with radius (the physical radius is calculated assuming an inclination of $77°$ and P.A. of $38°$; Fritz et al. 2011). In the star-forming ring at 10 kpc, β has an average value of $\sim$1.8 but increases with decreasing radius, reaching a maximum of $\sim$2.5 at a radius of $\sim$3 kpc. This is higher than found in global studies of galaxies (Planck Collaboration 2011a; Davies et al. 2012; Dunne et al. 2011). However, similarly high values have been reported recently in Foyle et al. (2012) and Bracco et al. (2011) for dust within galaxies. The value for the ring agrees well with early results from *Planck* (Planck Collaboration 2011a) for dust in the galactic disk and the solar neighborhood. The 10 kpc ring has an average dust surface density of $\sim$0.6 $M_\odot$ pc^{-2} with a dust temperature of 18 K. Toward the very center of the galaxy the dust column density decreases to $\sim$0.04 $M_\odot$ pc^{-2}, β values fall to $\sim$1.9, and the dust temperature increases to $\sim$30 K.

In Figure 8, we see a clear break in the radial variation for both temperature and β at a radius $\sim$3 kpc. We fit a model with two straight lines and a transition radius (using a simplex routine) to the β results. The same method is used with the temperature values but we set the transition radius to the value obtained from the fit to the β values, which occurs at 3.1 kpc (shown by the dashed green line in Figure 8 or black ellipse in Figure 7). At radii smaller than the transition radius, the temperature decreases with radius from $\sim$30 K in the center to $\sim$17 K, with an associated increase in β from $\sim$1.8 to $\sim$2.5. At radii larger than the transition radius the dust temperature slowly increases with radius while β decreases with radius to $\sim$1.7 at 13 kpc. The best-fit relationships between T_d, β, and R are shown in Figure 8 and listed below:

$$\beta = 0.15R\,(\text{kpc}) + 1.98 \quad R < 3.1\,\text{kpc} \tag{2}$$

$$= -0.08R\,(\text{kpc}) + 2.70 \quad 3.1 \leqslant R < 20\,\text{kpc} \tag{3}$$

$$T_d = -3.24R\,(\text{kpc}) + 27.56 \quad R < 3.1\,\text{kpc} \tag{4}$$
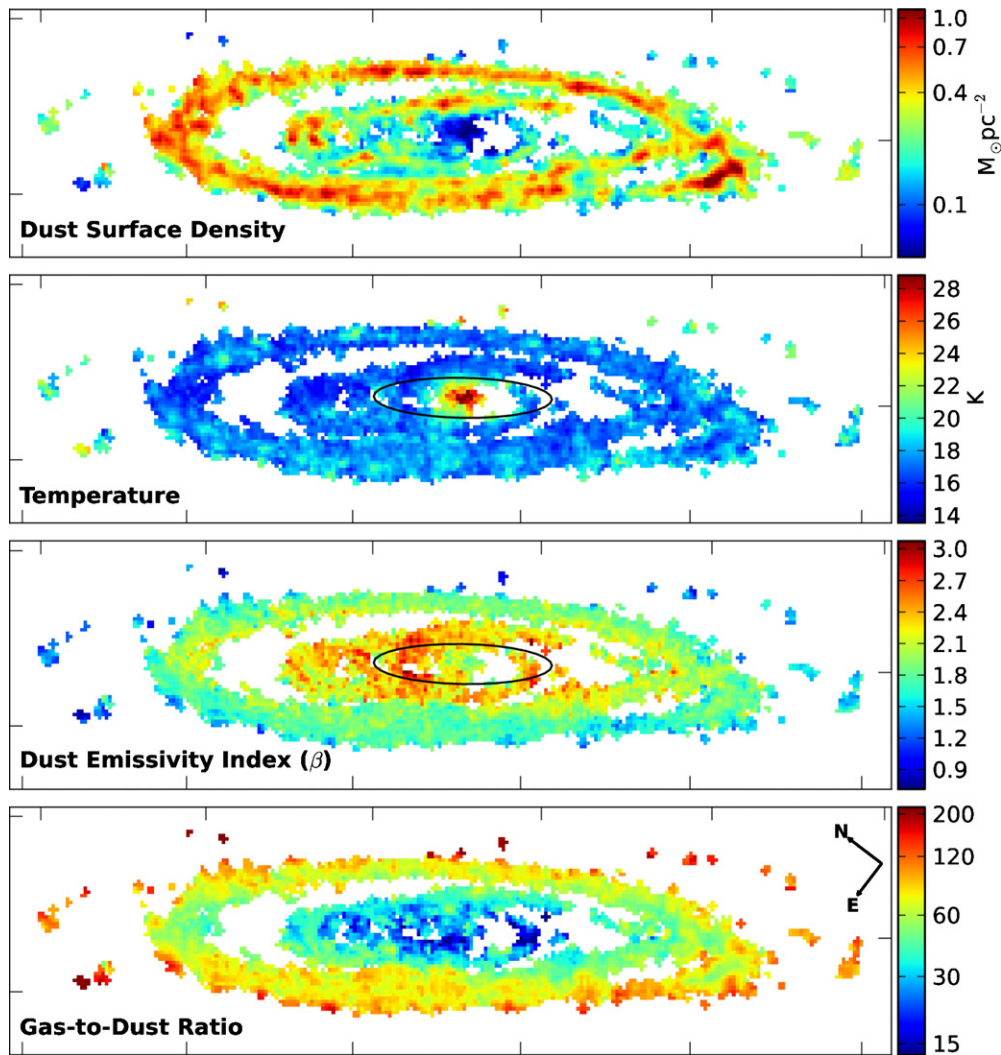
$$= 0.12R\,(\text{kpc}) + 16.40 \quad 3.1 \leqslant R < 20\,\text{kpc}. \tag{5}$$

We discuss the cause of the temperature and β variations in Section 5. For Sections 5.1 and 5.2, we consider the inner ($R < 3.1$ kpc) and outer regions separately.

4.2. Radial Distribution of Gas and Dust

In Figure 9 the radial variations of the atomic gas, the molecular gas, and the gas-to-dust ratio are shown. We assume

Figure 7. Distribution of dust surface density, temperature, and β obtained from the SED-fitting technique and the distribution of the gas-to-dust ratio. The temperature and β images include a black ellipse showing a radius of 3.1 kpc. The ticks are plotted at 30′ intervals.

(A color version of this figure is available in the online journal.)

an X-factor of $1.9 \times 10^{20} \, \mathrm{cm}^{-2} \, [\mathrm{K \, km \, s}^{-1}]^{-1}$ (Strong & Mattox 1996) to convert a CO line flux to an H_2 column density, although this value is notoriously uncertain and has been found to vary with metallicity (Strong et al. 2004; Israel 2005). For our analysis of M31, the choice of X-factor makes very little difference as the total gas is dominated by the atomic phase. Out of the 3974 pixels plotted in the gas-to-dust figure, only 101 have a molecular fraction of >50% and globally the molecular gas only constitutes ∼7% of the atomic gas (Nieten et al. 2006). To estimate the total gas surface density we include the contribution of the atomic or molecular gas in each pixel if the value is greater than 3σ in their respective maps. Only 86 of our 5σ dust pixels are not covered by the CO($J = 1$–0) observations; these pixels are in the outskirts of the galaxy and we assume that the contribution of molecular gas is negligible. We find a tight relation between the gas-to-dust ratio and radius (Spearman rank coefficient of 0.80) as shown in Figure 9, which is described by an exponential profile, shown by the red line.

The gas-to-dust ratio increases exponentially from low values of ∼20 in the center of the galaxy to ∼110 at 15 kpc typical of the MW in the local environment (see Devereux & Young 1990 and references therein). Note that the values are not cor-

rected for helium in the ISM. Metallicity gradients have been estimated from oxygen line ratios [O III]/Hβ, [O II]/[O III], and R_{23} by Galarza et al. (1999). They infer a radially decreasing metallicity gradient of -0.06 ± 0.03 dex kpc^{-1} from the R_{23} parameter. Trundle et al. (2002) calculate oxygen abundance gradients based on a set of 11 H II regions from Blair et al. (1982) and find gradients in the range of -0.027 to -0.013 dex kpc^{-1} depending on the calibration used. If a constant fraction of the metals in the ISM is incorporated into dust grains (Edmunds 2001), one would expect the gas-to-dust gradient to be -1 times metallicity gradient. We find a gas-to-dust gradient of 0.0496 ± 0.0005 dex kpc^{-1}, consistent within the uncertainties to the gradient measured by Galarza et al. (1999; if the H I map corrected for self-opacity is used the gradient slightly increases to 0.0566 ± 0.0007 dex kpc^{-1}). This supports the claim that gas can be well traced by dust at a constant metallicity. To see if the uncertainty in the choice of X-factor could affect this result, we carried out the same procedure but limited the analysis to pixels where the molecular hydrogen contribution is less than 10% of the total gas mass. This produced only a small change in the gas-to-dust gradient to 0.0550 ± 0.0007 dex kpc^{-1}, which is still consistent with the metallicity gradient.
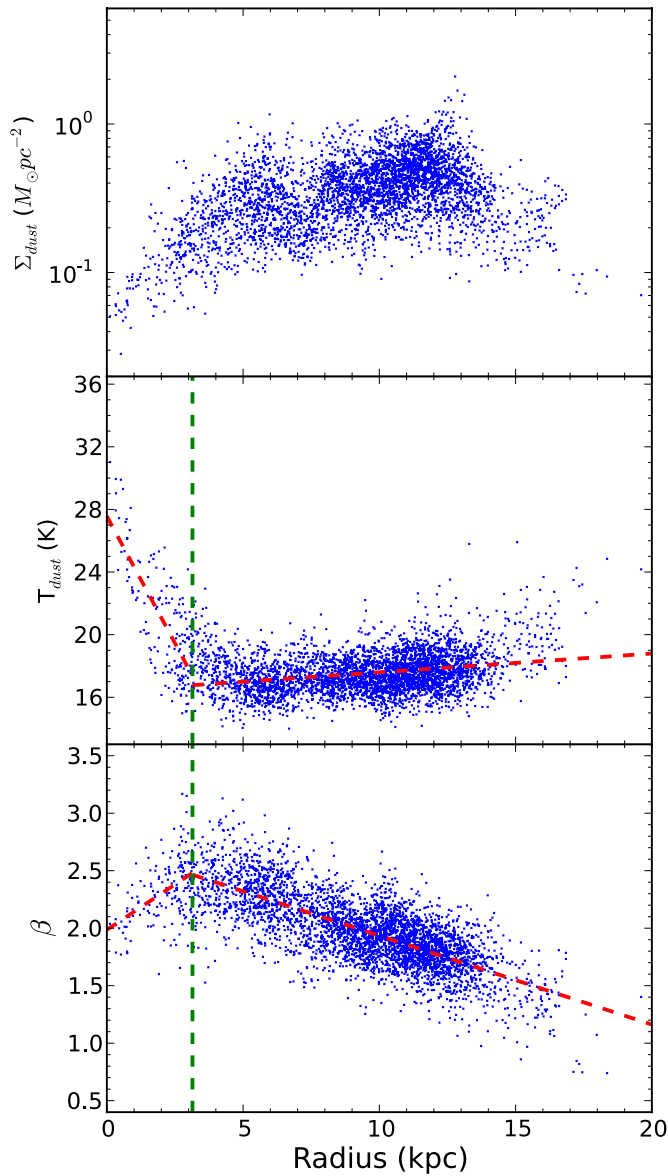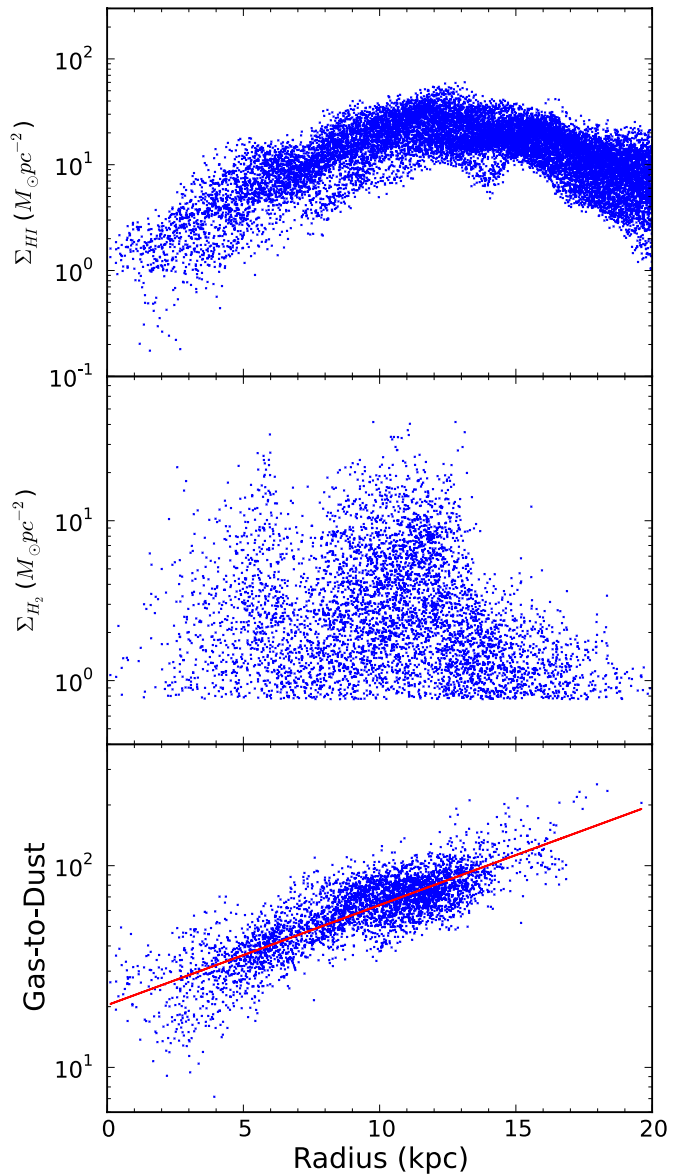
Figure 8. Results from the SED fits for each pixel plotted vs. radius. The dashed red lines represent the best-fit linear model (see Section 5.1), the dashed green line represents the transition radius (3.1 kpc) found when fitting the β results.

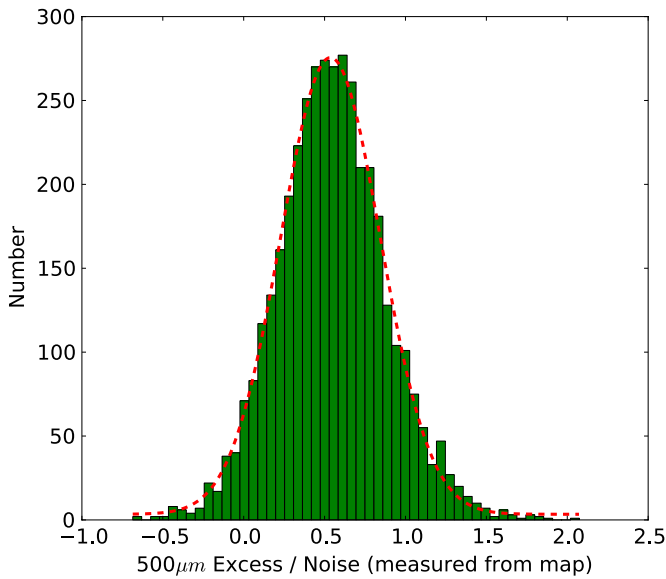(A color version of this figure is available in the online journal.)

Figure 9. Distribution of atomic gas, molecular gas, and gas-to-dust ratio vs. radius. The two gas maps are plotted for all pixels $>3\sigma$. The solid red line represents the best-fit exponential profile to the gas-to-dust ratio.

(A color version of this figure is available in the online journal.)

4.3. 500 μm Excess

Searches for a long-wavelength submillimeter excess (i.e., $>500\,\mu$m) has been made in both the MW (Paradis et al. 2012) and for nearby galaxies. A submillimeter excess is important as it could suggest that very cold dust is present ($<15\,$K) which would dominate the dust mass in galaxies. Other possible explanations of an excess include variations in the dust emissivity index with wavelength (Wright et al. 1991; Reach et al. 1995; Paradis et al. 2012), different dust populations, or contamination from a synchrotron radio source. Submillimeter excesses have been reported from observations of low-metallicity dwarf galaxies (see O'Halloran et al. 2010; Grossi et al. 2010; Dale et al. 2012) and spiral galaxies (see Zhu et al. 2009; Bendo et al. 2006). Most detections have been made by combining FIR data with ground-based data at $850\,\mu$m or 1 mm data rather than from data only at $\leqslant 500\,\mu$m.

We searched for a submillimeter excess in M31 by comparing the $500\,\mu$m flux to our best-fit models. A $500\,\mu$m excess is defined to be any observed $500\,\mu$m flux that is greater than the expected flux at $500\,\mu$m from our modified-blackbody fit to the data. Figure 10 is a histogram of the ratio of the excess at $500\,\mu$m and the noise on the $500\,\mu$m map. The distribution of the excess is consistent with a Gaussian function with a mean of 0.54σ and standard deviation of 0.31σ. The fact the distribution of the histogram is a Gaussian suggests that what we are seeing is random noise with a fixed offset (not centered on zero). Two non-astronomical sources could explain a fixed offset, either an incorrect background subtraction or a calibration error. The background correction applied is quite small (0.2σ), and thus an error in this is unlikely to be the entire explanation of the offset. The distribution of the excess is consistent with the 2% random SPIRE calibration uncertainty, so both factors together could explain the small offset. If the excess is generated from

Figure 10. Value of the 500 μm excess, defined as the 500 μm flux from our blackbody model, divided by the noise. The red line is a Gaussian fit to the histogram.

(A color version of this figure is available in the online journal.)

dust with a 10 K temperature and β of 2, the dust mass is $\sim 10^{6.58}\,M_\odot$ in our $>5\sigma$ pixels, which corresponds to only 13% of the mass of the warmer dust. If we used a model containing dust at more then one temperature we would not get a useful constraint on the colder dust component without additional data at longer wavelengths. In particular observations at $\sim 850\,\mu$m (e.g., with SCUBA2) would be useful to determine if any cold dust present.

5. DISCUSSION

5.1. Heating Mechanisms and Dust Distribution

Recent studies by Bendo et al. (2010, 2012) and Boquien et al. (2011) have used *Herschel* colors to confirm the findings of previous works (e.g., Lonsdale Persson & Helou 1987; Walterbos & Greenawalt 1996) that emission from dust in nearby galaxies at wavelengths longer than 160 μm is mostly from dust heated by the general stellar population. These authors conclude that at wavelengths shorter than 160 μm, the emission tends to be dominated from warmer dust heated by newly formed stars. Montalto et al. (2009) in a study of M31 using *Spitzer* MIR/FIR, UV, and optical data also concluded that the dust is mostly heated by an old stellar population (a few Gyr old). To investigate the relation between our derived dust properties and the SFR and the general stellar population, we have used the 3.6 μm map presented in Barmby et al. (2006) to trace the general stellar population (rather than the luminous newly formed stars that dominate the UV) and a map of SFR. The SFR map is created from far-UV and 24 μm images that have been corrected for the contribution of the general stellar population to the emission at these wavelengths (for details see G. P. Ford et al., in preparation). These maps were all convolved to the same resolution and binned to the same pixel size as all the other maps in our analysis.

We have plotted the fluxes from these maps against the results of our SED fits (see Figure 11). In Section 4.1, we showed that there is a clear break in the dust properties at a radius of 3.1 kpc. Therefore in Figure 11 the pixels at a radius less than 3.1 kpc

Table 1
Spearman Correlation Coefficients for Properties of M31

Property A	Property B	Region	Spearman Coefficient	P-value
Dust Surface Density	3.6 μm flux	Inner	−0.73	1.52×10^{-28}
		Outer	−0.16	1.53×10^{-22}
	SFR	Inner	0.31	6.38×10^{-5}
		Outer	0.74	0.00
Temperature	3.6 μm flux	Inner	0.90	6.17×10^{-59}
		Outer	−0.09	7.46×10^{-9}
	SFR	Inner	0.04	5.97×10^{-1}
		Outer	0.14	3.70×10^{-19}
β	3.6 μm flux	Inner	−0.52	8.78×10^{-13}
		Outer	0.56	8.99×10^{-311}
	SFR	Inner	0.16	3.58×10^{-2}
		Outer	−0.24	2.85×10^{-52}

Notes. The Spearman rank-order correlation coefficient and *P*-value (for the null hypothesis that the two data sets are uncorrelated) for the scatter plots shown in Figure 11 (values were calculated using the scipy.stats package and checked with IDL r_correlate routine). The inner and outer regions contain 164 and 3810 pixels, respectively.

are shown in blue and those at a radius above 3.1 kpc in green. For each graph (and both sets of pixels) the Spearman rank coefficient is computed and an estimate made of its significance (see Table 1). With such a large number of pixels, all but one of our correlations are formally significant. In the discussion below, we have concentrated on the strongest correlations as measured by the Spearman correlation coefficient.

There are strong correlations in Figure 11 between β and 3.6 μm emission. We believe these are most likely to be caused by radial variations in β seen in Figure 8 and the decrease in 3.6 μm brightness with radius. We discuss the possible cause of the radial variation in β in Section 5.2.

We find a strong correlation between dust surface density and the SFR in the outer regions, but not with the surface density of total stars traced by the 3.6 μm emission. This correlation is expected as stars are formed in clouds of gas and dust. In the inner region, there is an anti-correlation between the dust surface density and the 3.6 μm flux, which seem most likely to be explained by both quantities varying with radius: the 3.6 μm emission from the bulge increasing toward the center and the dust surface density decreasing toward the center.

The strongest correlation is seen between the dust temperature and the 3.6 μm flux in the inner region. Figure 12 shows a log–log graph of the two quantities and a linear fit to the points. The gradient represents the power n where $F_{3.6\,\mu\mathrm{m}} \propto T_{\mathrm{dust}}^n$ where $n = 4.61 \pm 0.15$. While the correlation suggests the dust in the bulge is heated by the general stellar population, for a modified blackbody with $\beta = 2$ we would expect a gradient of 6. The difference is probably explained by the simplicity of our assumptions: that there is only a single stellar population in the bulge and that the bulge has a constant depth in the line of sight (LOS). If these assumptions are incorrect, the 3.6 μm surface brightness of M31 will only be an imperfect tracer of the intensity of the interstellar radiation field (ISRF).

Looking at the temperature beyond 3.1 kpc, we find a weak, but still highly significant, correlation with SFR, suggesting that the ISRF has a significant contribution from star-forming regions. As most of the star formation in M31 occurs in the 10 kpc ring, this is to be expected. This correlation can be seen in Figure 13 where most but not all of the temperature peaks in the
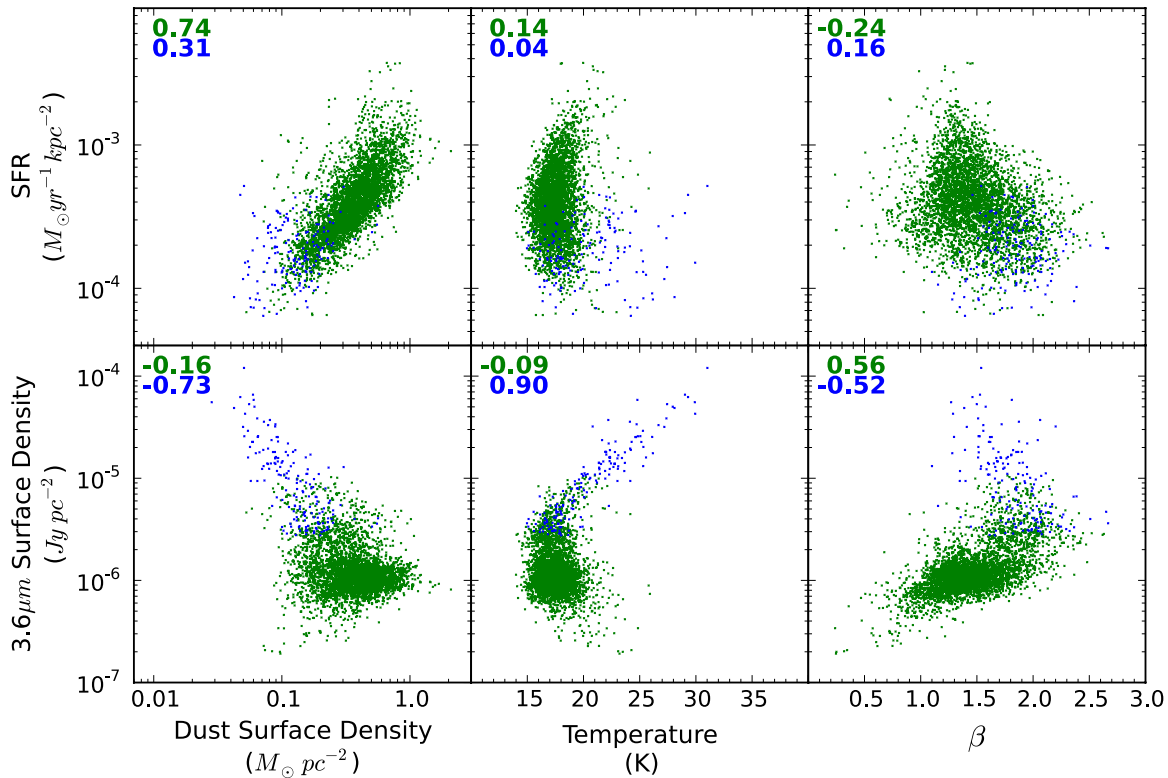
Figure 11. Scatter plots showing correlations between dust properties and 3.6 μm flux or SFR. The blue points are results at radii <3.1 kpc and the green data points are results at radii >3.1 kpc. The Spearman rank-order coefficients for both sets of points are shown in the top left corner of each plot.

(A color version of this figure is available in the online journal.)
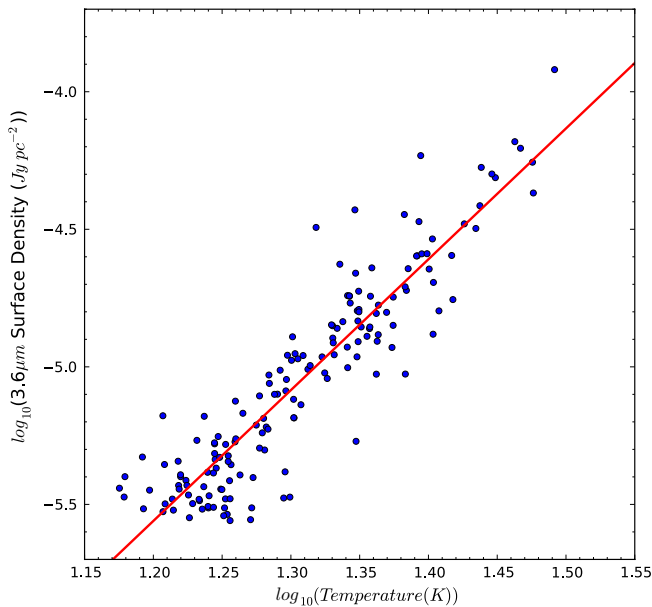
Figure 12. Log(3.6 μm) flux vs. log(Temperature) for the inner 3.1 kpc. The best-fit linear model is shown by the red line.

(A color version of this figure is available in the online journal.)

10 kpc ring appear aligned with the peaks in the SFR map. In the same region there is a slight anti-correlation of temperature with the 3.6 μm flux which could be explained by the radial decrease in the 3.6 μm flux while the dust temperature increases slightly with radius. The fact that dust temperature increases slightly with radius, while the number-density of stars, traced by the 3.6 μm, is falling with radius suggests that outside the bulge the dust is mainly heated by young stars. Nevertheless, the lack of a strong correlation between dust temperature and either SFR or 3.6 μm flux suggests that the optical/UV light absorbed by a dust grain is from photons from a large range of distances (e.g., photons from the bulge heating dust in the disk).

Bendo et al. (2012) have studied FIR color ratios in M81, M83, and NGC 4203. They find the 250/350 μm color ratio has the strongest positive correlation with 1.6 μm emission. An increase in the 250/350 μm ratio would indicate either an increase in dust temperature or a decrease of β. Bendo et al. (2012) conclude that the most likely explanation is the temperature effect, with the dust being heated by the general stellar population traced by the 1.6 μm emission. We find a similar correlation to Bendo et al. (2012), only we trace the stellar radiation field with the 3.6 μm band. However, our SED-fitting results suggest that this is caused by a combination of changes in temperature and β. Note that since Bendo et al. (2012) only use color ratios they are unable to discriminate between changes of temperature and β. At radii greater than 3.1 kpc our results suggest that the variation in the 250/350 μm is mainly caused by a change in β. Bendo et al. (2012) found that the 70/160 μm color ratio has the greatest correlation with SFR, which is evidence that there is dust at more than one temperature contributing to the 70–500 μm emission. One possible explanation of our failure to find a correlation between the 3.6 μm emission and dust temperature outside 3.1 kpc, instead of the negative correlation between 3.6 μm and β we find, might be if the *Herschel* emission at short wavelengths contains a contribution from a warmer dust component. This would mean that
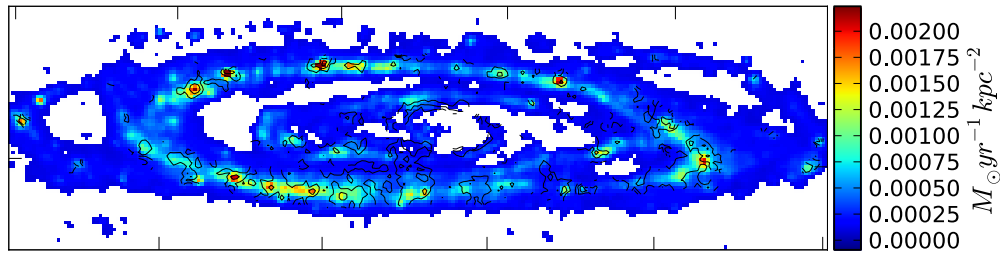
Figure 13. Color image shows the SFR image from G. P. Ford et al. (in preparation) which has been smoothed and re-gridded to match the maps presented in Figure 7. The contours are from the dust temperature map and drawn at 18.0, 19.5, and 21.0 K values.

(A color version of this figure is available in the online journal.)

our fits of a one-component modified blackbody would produce misleading results. However, as stated in Section 3.1 when we attempted the same SED-fitting process but using all flux densities $\leqslant 160\,\mu$m as upper limits, we see little difference in our results.

5.2. Dust Emissivity and Temperature Relation

The dust emissivity index (β) is related to the physical properties of the dust grains, including the grain composition, grain size, the nature of the absorption process, and the equilibrium temperature of the dust. We would also expect to see a change in β due to environment from the processing of the grains via grain growth (e.g., coagulation, mantle accretion) or destruction through surface sputtering by ions/atoms or shattering by shocks. In M31, we detect an apparent inverse correlation between T_d and β for the inner and outer regions of M31, as shown in Figure 14. We find that the form of the relation is different for the two regions.

Such an inverse relationship has been observed in the MW with previous FIR–submillimeter experiments and surveys including ARCHEOPS (Désert et al. 2008), which showed β ranging from 4 to 1 with the dust temperature varying between 7 and 27 K, and PRONAOS (Dupac et al. 2003), which shows a variation of β from 2.4 to 0.8 for dust temperatures between 11 and 80 K. Veneziani et al. (2010) used IR-mm data of Galactic high latitude clouds and found a similar trend, and more recently Paradis et al. (2010) with *Herschel* found a similar inverse relationship with $\beta = 2.7$–1.8 for $T_d = 14$–21 K for galactic longitude 59° (at longitude 30° $\beta = 2.6$–1.9 for 18–23 K). Recently Bracco et al. (2011) used *Herschel*-ATLAS observations to investigate β variations in low-density, high-latitude galactic cirrus, measuring values of β ranging from 4.5 to 1.0 for $10 < T_d < 28$ K. These T_d–β relationships could be indicative of a problem with the temperature–β degeneracy arising from the SED fitting, the presence of dust with a range of temperatures along the LOS (Shetty et al. 2009b), or real variations of the properties of the dust grains.

On the assumption that the inverse correlations between β and T_d in Figure 14 are not simply caused by the two variables being separately correlated with radius, we looked for other possible causes of the relationships.

1. The fitting can lead to a spurious inverse correlation between β and T_d (Shetty et al. 2009a, Section 3.3). The most striking feature in Figure 14 is the clear separation in points between the inner 3.1 kpc and the outer regions. To test whether these different distributions might be produced by the fitting artifact, we used the Monte Carlo simulations from Section 3.3 to simulate the effect of fitting a modified

blackbody for various combinations of β and T_d. The gray lines in Figure 15 show the best-fit relationships for different input T_d and β combinations and clearly show that the two different relationships in the two regions cannot be obtained from a single population of dust grains. The green and blue data points represent the range of output T_d and β for an input modified blackbody with $T = 17.0$ K (green) and $T = 25.0$ K (blue), with $\beta = 2.0$. A comparison of Figures 14 and 15 shows that in both regions of M31 there is a larger range of temperature and dust emissivity for the real data than that found in the Monte Carlo simulation, indicating there are genuine variations of T_d and β in both regions. Moreover, the fitting artifact cannot explain the observed relationships of β and temperature with radius (Figure 8).

2. Artificial inverse T_d–β relationships can also be produced if a one-component modified-blackbody model is used to fit dust which contains a range of dust temperatures (Shetty et al. 2009b). Since we are averaging through the disk of a galaxy along the LOS, it is obviously possible that the dust contains a range of dust temperatures. While we cannot fully address this issue, our β values are higher than expected, which is the opposite of what happens from an LOS averaging of temperatures. We also find no statistical evidence from our fits that there is more than one component of dust. Also, Paradis et al. (2010) and Anderson et al. (2010) show that inverse T_d–β relationships still exist in places where it is unlikely there is dust at more than one temperature.

3. Variation of β with wavelength has been reported by some authors both from theoretical models and laboratory experiments and from observations (e.g., Meny et al. 2007; Coupeaud et al. 2011), with a transition around 500 μm. In Section 4.3, we show that there is no evidence for excess 500 μm emission, suggesting that this is not an explanation of our results.

To describe the T_d–β relationships we use an empirical model of the form $\beta = AT^\alpha$, commonly used in the literature (e.g., Désert et al. 2008; Paradis et al. 2010; Planck Collaboration et al. 2011) to fit the T_d–β anti-correlation. The observed anti-correlation between T and β may arise due to a change in the physical properties of grains including the grain optical constants changing with temperature for amorphous grains or changes in the dust emissivity with wavelength (see Ysard et al. 2012, and references therein). Other possibilities include grain growth or quantum mechanical effects (though these latter grain properties only arise at lower dust temperatures than observed in M31). The best-fit relationship which describes T_d–β for
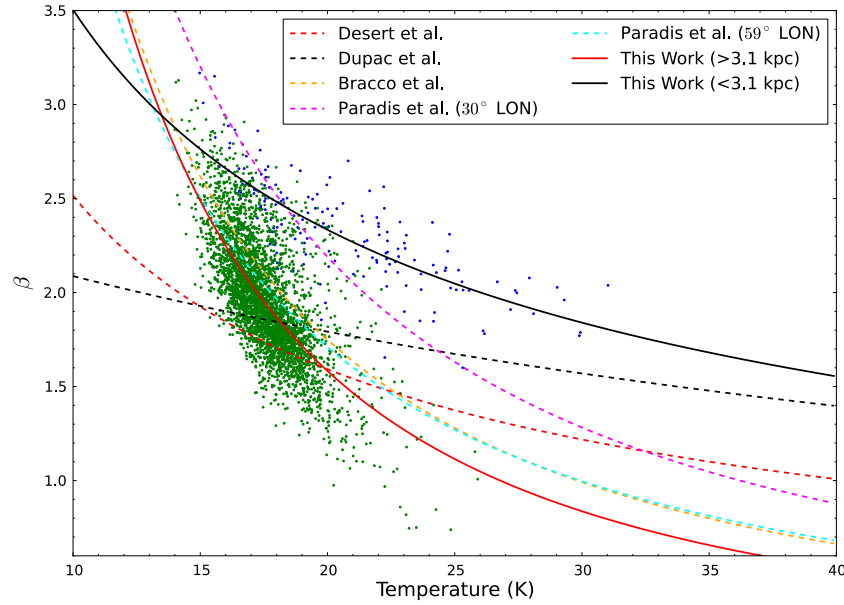
Figure 14. Variation of the dust temperature with emissivity index across M31. Data points are color coded for those within $R < 3.1$ kpc (blue) and those beyond this radius (green). Solid lines show the best-fit relations for T_d–β in M31. The T_d–β relationships in the literature are indicated by the dashed lines (including Dupac et al. 2003; Désert et al. 2008; Paradis et al. 2010; Bracco et al. 2011).

(A color version of this figure is available in the online journal.)
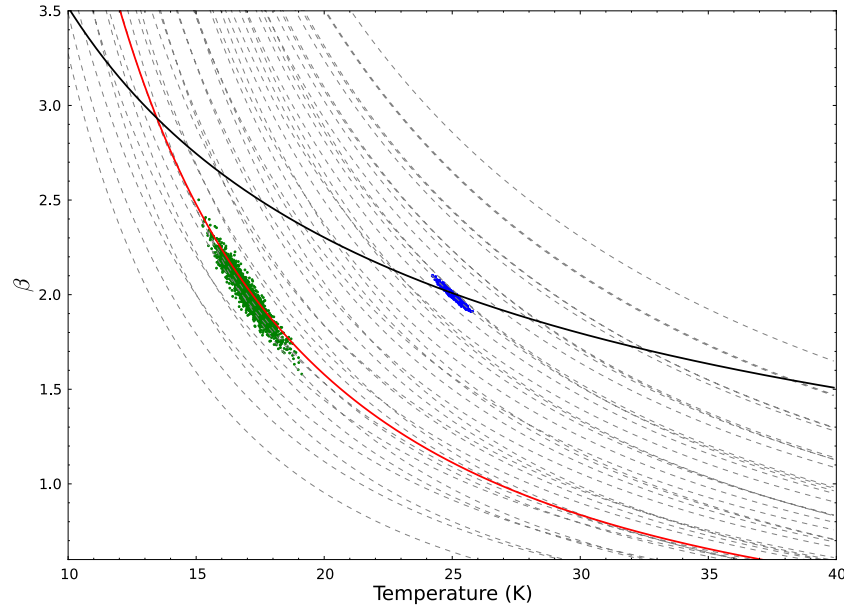
Figure 15. Variation of the dust temperature with emissivity index that arise from just the uncertainties in the measurements. The data shown use the simulations of the SED-fitting method, described in Section 3.3. The green and blue data points show the recovered values of β and T_d for an input model with $T = 17.0$ K, $\beta = 2.0$ (green) and $T = 25.0$ K, $\beta = 2.0$ (blue). We have carried out the same simulation for input values of T_d and β over the range T_d of 15–29 K in 2 K intervals and in β of 1.6–2.4 in 0.2 intervals. For each group of points we have fitted a line $T_d \propto \beta^n$, which are the gray dashed lines. In these cases we have not shown the recovered values of T_d and β, merely the lines that are the best fit to the points. The red and black solid lines are the best-fit models to the real data as shown in Figure 14. When compared with Figure 14 it is clear that the uncertainties cannot account for the distribution in the real data.

(A color version of this figure is available in the online journal.)

$R < 3.1$ kpc and for $3.1 < R < 15$ kpc is (shown in Figure 14)

$$\beta = \begin{cases} 2.30 \left(\dfrac{T_d}{20}\right)^{-0.61} & R < 3.1 \text{ kpc} \\[2ex] 1.58 \left(\dfrac{T_d}{20}\right)^{-1.57} & 3.1 \leqslant R < 15 \text{ kpc,} \end{cases} \qquad (6)$$

where the steeper T_d–β relationship at $R > 3.1$ kpc agrees well with the relationship found in the plane of the MW at longitudes of 59° (Paradis et al. 2010) and in low-density, high-latitude cirrus (Bracco et al. 2011). There is some evidence that the T_d–β relationship in M31 is slightly steeper, so that for the same temperature compared to the galactic plane, M31 has a lower β (but this is only at ~5%–10% level).

13

What could be a physical (or chemical) explanation of the different β–T_d relationships in the two regions? Typical values of β are in the range 1.5–2.0 for interstellar dust grains and have been found in global extra-galactic studies (e.g., Skibba et al. 2011; Smith et al. 2012; Dunne et al. 2011) and *average* global values measured in the MW (e.g., Paradis et al. 2010; Bracco et al. 2011; Planck Collaboration 2011c). Low values of β for large grains would typically represent freshly formed dust grains in circumstellar disks or stellar winds. Alternatively, $\beta \sim 1$ has been observed in regions where small grains dominate (Seki & Yamamoto 1980). High values of β (>2) might occur due to grain coagulation or to the growth of icy mantles on the surface of the grains in denser regions (Aannestad 1975; Lis et al. 1998; Stepnik et al. 2003). Studies have also suggested that high values of β are associated with very cold dust ($T < 12$ K; e.g., Désert et al. 2008) possibly caused by a change in the absorption properties due to quantum effects at low temperatures, increasing self-absorption in amorphous grains via tunneling (Agladze et al. 1996; Mennella et al. 1998; Meny et al. 2007; Paradis et al. 2012).

The highest value of β is seen at the 3.1 kpc boundary between the two regions. This cannot be caused by changes in the quantum mechanical absorption, since this is only thought to be important for cold dust at temperatures <12 K. The high β values could be due to efficient grain coagulation or mantle growth in dense molecular clouds, although this too seems unlikely as little CO($J = 1$–0) is observed in this region. While there is no obvious explanation for the high β values at this radius, there are many indications that this 3 kpc "boundary" is an interesting regime, we discuss this further in Section 5.3.

In the inner region, we suggest that the decrease in β with corresponding increase in T_d might be caused by the increased intensity of the ISRF. Toward the center of M31, we would expect increased sputtering or sublimation of mantles from the increased ISRF, shown by the increased temperature of the dust and the increased X-ray emission observed in the center (Shirey et al. 2001). The lack of gas in the central regions (Figure 9) also suggests that dust is less likely to be shielded and thus more efficiently sputtered and leading to smaller grain sizes.

As we mentioned above, a problem with this analysis is that it is difficult to determine which are the causal relationships. For example, we have argued that the radial variation in T_d is due to the radial variation in the ISRF. The radial variation in β might then be due to a physical relationship between T_d and β or it might be the case that there is no causal relationship between these parameters but the radial variation in β is caused by a different effect. For example, an interaction between M32 and M31 might have caused a wave of star formation that has moved out through the galaxy, which might have led (by a number of processes) to the radial variations in β. Therefore, we can rule out some hypotheses but we cannot conclusively determine which is the true explanation using this data set.

5.3. Why a Transition at 3.1 kpc?

Interpreting the transition in dust properties seen at 3.1 kpc (Figure 8) is difficult. One possible clue comes from previous gas kinematics studies. Chemin et al. (2009) found that the H I rotation curve inside a 4 kpc radius is warped with respect to the rest of disk. Stark & Binney (1994) suggest that the inner H I data are consistent with a bar extended to 3.2 kpc, while a newer analysis by Berman (2001) explains the H I distribution as the result of a triaxial rotating bulge. Block et al. (2006), using *Spitzer*/IRAC observations, identified a new inner dust

ring with dimensions of 1.5×1 kpc. By using the stellar and gas distributions and from the presence of the 10 kpc ring, they conclude that an almost head-on collision occurred between M31 and M32 around 210 million years ago. This collision could explain the perturbation of the gas observed in the central 4 kpc. These other observations all show that the inner 3 kpc of M31 is an intriguing region, although it is not clear what are the causes of the difference in the dust properties. The perturbation of the gas may have lead to the processing of dust grains, or potentially material from M32 could have been deposited after the interaction. The total dust mass for the pixels in our selection within 3.1 kpc is $10^{4.2}\ M_\odot$ which is a plausible amount to be deposited as recently dust masses of $\sim 10^5\ M_\odot$ have been reported in Virgo dwarf ellipticals (Grossi et al. 2010).

Another possibility is that the dust properties are affected by the differences between conditions in the bulge and disk. Courteau et al. (2011) decomposed the luminosity profile of *Spitzer*/IRAC data into a bulge, disk, and halo. From their Figure 16, we can see that our transition radius of ~ 3 kpc is approximately where the bulge emission begins to become a significant fraction of the optical disk emission. Whether the transition in the dust parameters is due to the changing contribution to the ISRF from the general stellar population and star formation or if there is another influence in the bulge is unknown.

5.4. Dark Gas and X-factor

The detection of "dark gas" in the MW was a surprising early result from Planck (Planck Collaboration 2011a), obtained by combining *IRAS* 100 μm data and the six-band *Planck* data from 350 μm to 3 mm. The *Planck* team compared the dust optical depth with the total column density of hydrogen ($N_{\rm H}^{\rm Tot}$), where the optical depth at each wavelength is given by

$$\tau_\nu = \frac{I_\nu}{B(\nu, T_{\rm dust})}, \qquad (7)$$

where I_ν is the flux density in that band and $B(\nu, T_{\rm dust})$ is the blackbody function. They assumed that at low $N_{\rm H}^{\rm Tot}$ the atomic hydrogen dominates over the molecular component while at high column density the molecular hydrogen dominates the emission. For these two regimes they found a constant gas-to-dust ratio, but at intermediate column densities they found an excess of dust compared to the gas. This excess is attributed to gas traced by dust but not by the usual H I and CO lines, and is found to be the equivalent 28% of the atomic gas or 118% of the molecular gas. The excess dust emission was typically found around molecular clouds, suggesting that the most likely cause is the presence of molecular gas not traced by the CO line.

We attempted the same analysis as the Planck Collaboration (2011a) for M31 using our SED-fitting results from Section 4. Instead of using Equation (7), we compare the column density of gas estimated from the H I and CO with the column density of dust (for convenience we call this $\Sigma_{\rm dust}$). We use this parameter as it is calculated with data from all wavelengths, whereas if we used Equation (7), small errors in temperature would cause large uncertainties in τ_ν for wavelengths close to the peak of emission.

The *Planck* team found no radial variation in the gas-to-dust ratio in the MW (see Figure 10; Planck Collaboration 2011b). In Andromeda, we show that the gas-to-dust ratio does vary radially (Section 4.2 and Figure 9), as expected from the metallicity gradient. To determine if there is an excess at
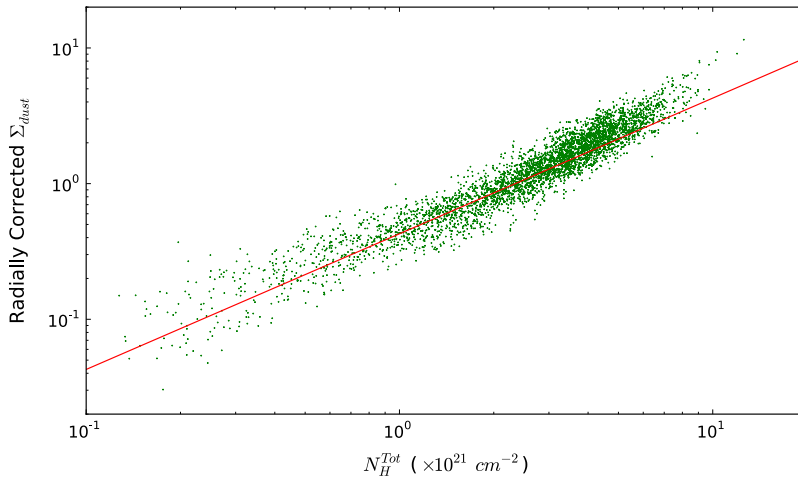
Figure 16. Radially corrected Σ_{dust} vs. total column density of gas. The plot is shown using our best-fit value of the X-factor of $(1.9 \pm 0.4) \times 10^{20}$ cm^{-2} [K km s^{-1}]$^{-1}$. The red line represents the best-fit model to the data assuming that $\Sigma_{dust} \propto N_H^{Tot}$. The plot shows that, unlike the *Planck* data for the Milky Way (Planck Collaboration 2011a), at intermediate gas column densities we do not find an excess in dust column density over the best-fit model, which would indicate the presence of gas not traced by the H I and CO ("dark gas").

(A color version of this figure is available in the online journal.)
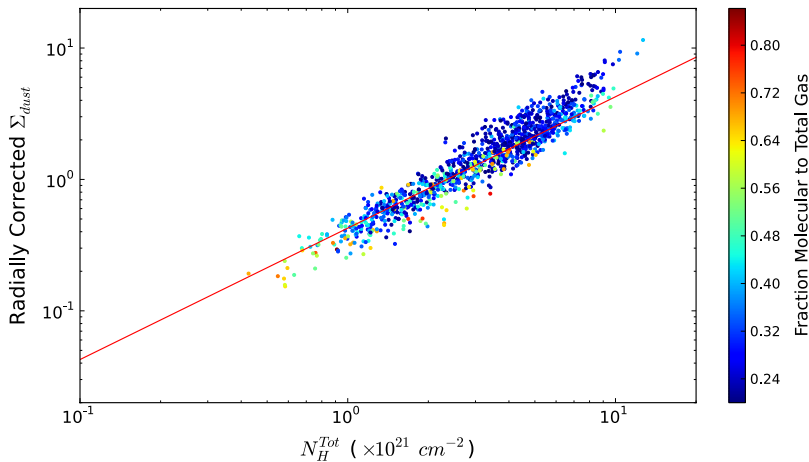
Figure 17. Radially corrected Σ_{dust} vs. column density of gas for pixels where the molecular fraction is greater than 20%. The data points are color coded with the fraction of molecular gas compared to total gas. The figure shows that the high column densities are not dominated by regions of molecular gas traced by the CO. The red line is the fitted model from Figure 16.

(A color version of this figure is available in the online journal.)

intermediate column density in dust compared to that expected from the gas we have to correct for the radial change in gas-to-dust ratio. To remove this dependence, we adjust dust column density by using the exponential fit (shown by the red line in Figure 9) so the gas-to-dust ratio at all radii has the same value as the center of M31. To avoid biasing this correction by assuming a value for the X-factor which is highly uncertain, we estimate this relationship from pixels where the atomic hydrogen column density is >95% of N_H^{Tot} (1569 pixels out of the 3600).

In Figure 16, we show that the relationship between corrected dust column density (Σ_{dust}) and gas column density is well represented by assuming that the two quantities are directly proportional with no excess in dust column density that could be attributed to "dark gas." Although only a small proportion of the gas is molecular, we still need to use a value for the X-factor. We can estimate this quantity from the data itself by finding the values of the X-factor and the constant of proportionality between the gas column density and the corrected Σ_{dust} that gives the minimum χ^2 value (the fitted line is shown in Figure 16). We find a best value for the

X-factor of $(1.9 \pm 0.4) \times 10^{20}$ cm^{-2} [K km s^{-1}]$^{-1}$ (or expressed as $\alpha_{CO} = 4.1 \pm 0.9\ M_\odot$ pc^{-2} [K km s^{-1}]$^{-1}$), where the random error is estimated using a Monte Carlo technique (similar to one used in Section 3.1). For the dust column densities in each pixel we use the uncertainties provided by the SED fitter as explained in Section 3.1, which is on average $\sim$22%. Nieten et al. (2006) quote a calibration error of 15% for the CO observations (which directly results in at least a 15% uncertainty in the X-factor), which we combine with the noise in each pixel of our processed moment-zero CO map. For the H I observations we use an uncertainty map provided by R. Braun (2012, private communication), which has an average uncertainty of 12% on the raw 10$''$ map. We also include a 5% systematic uncertainty (e.g., calibration uncertainties). If the opacity corrected H I map is used our best-fit X-factor is $(2.0 \pm 0.4) \times 10^{20}$ cm^{-2} [K km s^{-1}]$^{-1}$.

Leroy et al. (2011) find values of the X-factor between 0.97 and 4.6×10^{20} cm^{-2} [K km s^{-1}]$^{-1}$ when analyzing the southern, northern, and inner regions for M31 with *Spitzer* data. Our average value of the X-factor falls within their range of values.
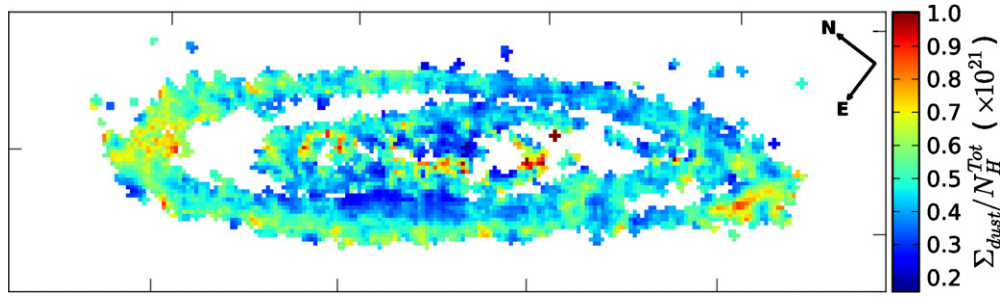
Figure 18. Map of $\Sigma_{\mathrm{dust}}/N_{\mathrm{H}}^{\mathrm{Tot}}$ ratio in M31. Higher values represent areas where there is less gas than predicted from dust measurements. The tick spacing represents $30'$.

(A color version of this figure is available in the online journal.)

A full analysis of the spatial variations of the X-factor with our data will be undertaken in a future paper.

There are two main problems with this method which could lead us to miss "dark gas." First, unlike the MW we have to average through the whole disk of M31, and second, M31 has a significantly lower molecular gas fraction. The latter prevents us from fitting the model to pixels with just very high and low values of $N_{\mathrm{H}}^{\mathrm{Tot}}$ as the pixels with highest molecular gas fraction are not clustered to high N_{H} values (this is illustrated in Figure 17). This suggests Andromeda may not be the best galaxy for this analysis as the molecular contribution to the overall column density is quite low.

However, we can also try an alternative method of looking for "dark gas" because we have one important advantage over the *Planck* team: we can see M31 from the outside. We can therefore make a map of the ratio of radially corrected dust column density (Σ_{dust}) to gas column density to look for regions of enhancements in this ratio (Figure 18). The image clearly shows spatial variations which could either suggest regions of "dark gas" or local variations in the metallicity or emissivity of dust. To distinguish between these scenarios an independent measurement of the "dark gas" is required. On the outskirts of molecular clouds, CO could be photodissociated and the carbon gas would therefore reside in C or C^+ (Wolfire et al. 2010). Planned observations of the C[II] $158\,\mu$m line in Andromeda with *Herschel* could then be a potential test for investigating whether "dark gas" exists in M31.

6. CONCLUSIONS

In this paper, we present the results of an analysis of dust and gas in Andromeda using new *Herschel* observations from the HELGA survey. We have $\sim$4000 independent pixels with observations in the range of 70–500 μm. We find the following results.

1. We find that a variable dust emissivity index, β, is required to adequately fit all the pixels in Andromeda. When a variable β is used, the modified-blackbody model with a single temperature is found to be a statistically reasonable fit to the data in the range 100–500 μm. There is no significant evidence of an excess of dust emission at 500 μm above our model.

2. There are two distinct regions with different dust properties, with a transition at $R = 3.1$ kpc. In the center of Andromeda, the temperature peaks with a value of $\sim$30 K and a β of $\sim$1.9. The temperature then declines radially to a value of $\sim$17 K at 3.1 kpc with a corresponding increase in β to $\sim$2.5. At radii larger than 3.1 kpc β declines but only with a small associated increase in temperature.

3. The drop in β toward the center of the galaxy may be caused by increased sputtering or sublimation of mantles from an increased ISRF. The origin of the high β values at 3.1 kpc from the center is less clear but may be indicative of either grain coagulation or an increase in the growth of icy mantles.

4. The dust surface density for our pixels in which flux is detected at $>5\sigma$ in all *Herschel* bands range is between $\sim$0.1 and 2.0 $M_\odot$ pc^{-2}. We find that the gas-to-dust ratio increases exponentially with radius. The gradient matches that predicted from the metallicity gradient assuming a constant fraction of metals are included into dust grains. The dust surface density is correlated with the SFR rather than with the stellar surface density.

5. In the inner 3.1 kpc the dust temperature is correlated with the 3.6 μm flux. This suggests that the heating of the dust in the bulge is dominated by the general stellar population. Beyond 3.1 kpc there is a weak correlation between dust temperature and the SFR.

6. We find no evidence for "dark gas," using a similar technique as the *Planck* team. However, we find this technique may not be as effective for M31 due to poor angular resolution and LOS effects. We have used an alternative technique by constructing a gas-to-dust map after correcting for the radial gradient. We do find regions with enhancements (i.e., higher values of $\Sigma_{\mathrm{dust}}/N_{\mathrm{H}}^{\mathrm{Tot}}$), which may show places where "dark gas" exists, or may be due to local variations in the gas-to-dust ratio. A detection of a potential component of CO-free molecular gas will be possible with future observations to measure the C[II] line planned with *Herschel*.

7. By minimizing the scatter between our radially corrected dust column density and the column density of gas inferred from the H I and CO line we find a value for the X-factor of $(1.9 \pm 0.4) \times 10^{20}$ cm^{-2} [K km s^{-1}]$^{-1}$ (or expressed as $\alpha_{\mathrm{CO}} = 4.1 \pm 0.9\, M_\odot$ pc^{-2} [K km s^{-1}]$^{-1}$).

Our results of Andromeda represent the largest resolved analysis of dust and gas in a single galaxy with *Herschel*. The results of this analysis on M31 is strikingly different from those obtained by the *Planck* team in the MW, since we find no clear evidence for "dark gas," a radial gradient in the gas-to-dust ratio, and evidence for radial variation in the dust emissivity index (β). In future work, it will be important to understand these differences between the two big spirals in the local group.

Facilities: Herschel (PACS and SPIRE), *Spitzer* (MIPS)

REFERENCES

Aannestad, P. A. 1975, ApJ, 200, 30
Abdo, A. A., Ackermann, M., Ajello, M., et al. 2010, ApJ, 710, 133
Agladze, N. I., Sievers, A. J., Jones, S. A., Burlitch, J. M., & Beckwith, S. V. W. 1996, ApJ, 462, 1026
Anderson, L. D., Zavagno, A., Rodón, J. A., et al. 2010, A&A, 518, L99
Barmby, P., Ashby, M. L. N., Bianchi, L., et al. 2006, ApJ, 650, L45
Bendo, G. J., Boselli, A., Dariush, A., et al. 2012, MNRAS, 419, 1833
Bendo, G. J., Buckalew, B. A., Dale, D. A., et al. 2006, ApJ, 645, 134
Bendo, G. J., Wilson, C. D., Pohlen, M., et al. 2010, A&A, 518, L65
Berman, S. 2001, A&A, 371, 476
Blain, A. W., Smail, I., Ivison, R. J., & Kneib, J.-P. 1999, MNRAS, 302, 632
Blair, W. P., Kirshner, R. P., & Chevalier, R. A. 1982, ApJ, 254, 50
Block, D. L., Bournaud, F., Combes, F., et al. 2006, Nature, 443, 832
Boissier, S., & Prantzos, N. 1999, MNRAS, 307, 857
Boquien, M., Calzetti, D., Combes, F., et al. 2011, AJ, 142, 111
Boselli, A., Lequeux, J., & Gavazzi, G. 2002, A&A, 384, 33
Boselli, A., Lequeux, J., & Gavazzi, G. 2004, A&A, 428, 409
Bournaud, F., Duc, P.-A., Brinks, E., et al. 2007, Science, 316, 1166
Bracco, A., Cooray, A., Veneziani, M., et al. 2011, MNRAS, 412, 1151
Braun, R., Thilker, D. A., Walterbos, R. A. M., & Corbelli, E. 2009, ApJ, 695, 937
Buat, V., Giovannoli, E., Takeuchi, T. T., et al. 2011, A&A, 529, A22
Calzetti, D. 2001, PASP, 113, 1449
Calzetti, D., Wu, S.-Y., Hong, S., et al. 2010, ApJ, 714, 1256
Chemin, L., Carignan, C., & Foster, T. 2009, ApJ, 705, 1395
Coupeaud, A., Demyk, K., Meny, C., et al. 2011, A&A, 535, A124
Courteau, S., Widrow, L. M., McDonald, M., et al. 2011, ApJ, 739, 20
Dale, D. A., Aniano, G., Engelbracht, C. W., et al. 2012, ApJ, 745, 95
Davies, J. I., Bianchi, S., Cortese, L., et al. 2012, MNRAS, 419, 3505
Désert, F.-X., Macías-Pérez, J. F., Mayet, F., et al. 2008, A&A, 481, 411
Devereux, N. A., & Young, J. S. 1990, ApJ, 359, 42
Draine, B. T. 2003, ARA&A, 41, 241
Draine, B. T., & Li, A. 2007, ApJ, 657, 810
Dunne, L., Gomez, H. L., da Cunha, E., et al. 2011, MNRAS, 417, 1510
Dupac, X., Bernard, J.-P., Boudet, N., et al. 2003, A&A, 404, L11
Eales, S., Smith, M. W. L., Auld, R., et al. 2012, ApJ, submitted (arXiv:1202.0547)
Eales, S. A., Smith, M. W. L., Wilson, C. D., et al. 2010, A&A, 518, L62

Edmunds, M. G. 2001, MNRAS, 328, 223
Foyle, K., Wilson, C. D., Mentuch, E., et al. 2012, MNRAS, 421, 2917
Fritz, J., Gentile, G., Smith, M. W. L., et al. 2011, A&A, submitted (arXiv:1112.3348)
Galarza, V. C., Walterbos, R. A. M., & Braun, R. 1999, AJ, 118, 2775
Gordon, K. D., Bailin, J., Engelbracht, C. W., et al. 2006, ApJ, 638, L87
Gordon, K. D., Engelbracht, C. W., Fadda, D., et al. 2007, PASP, 119, 1019
Gordon, K. D., Rieke, G. H., Engelbracht, C. W., et al. 2005, PASP, 117, 503
Grenier, I. A., Casandjian, J.-M., & Terrier, R. 2005, Science, 307, 1292
Griffin, M. J., Abergel, A., Abreu, A., et al. 2010, A&A, 518, L3
Grossi, M., Hunt, L. K., Madden, S., et al. 2010, A&A, 518, L52
Guelin, M., Zylka, R., Mezger, P. G., et al. 1993, A&A, 279, L37
Habing, H. J., Miley, G., Young, E., et al. 1984, ApJ, 278, L59
Hildebrand, R. H. 1983, Q. J. R. Astron. Soc., 24, 267
Israel, F. P. 2005, A&A, 438, 855
Kennicutt, R. C., Jr. 1998, ARA&A, 36, 189
Leroy, A. K., Bolatto, A., Gordon, K., et al. 2011, ApJ, 737, 12
Lis, D. C., Serabyn, E., Keene, J., et al. 1998, ApJ, 509, 299
Lonsdale Persson, C. J., & Helou, G. 1987, ApJ, 314, 513
McConnachie, A. W., Irwin, M. J., Ferguson, A. M. N., et al. 2005, MNRAS, 356, 979
Mennella, V., Brucato, J. R., Colangeli, L., et al. 1998, ApJ, 496, 1058
Mentuch, E., Wilson, C. D., Foyle, K., & Bendo, G. 2012, ApJ, submitted
Meny, C., Gromov, V., Boudet, N., et al. 2007, A&A, 468, 171
Montalto, M., Seitz, S., Riffeser, A., et al. 2009, A&A, 507, 283
Narayanan, D., Krumholz, M. R., Ostriker, E. C., & Hernquist, L. 2012, MNRAS, 421, 3127
Nieten, C., Neininger, N., Guélin, M., et al. 2006, A&A, 453, 459
O'Halloran, B., Galametz, M., Madden, S. C., et al. 2010, A&A, 518, L58
Ott, S. 2010, in ASP Conf. Ser. 434, Astronomical Data Analysis Software and Systems XIX, ed. Y. Mizumoto, K.-I. Morita, & M. Ohishi (San Francisco, CA: ASP), 139
Papovich, C., & Bell, E. F. 2002, ApJ, 579, L1
Paradis, D., Paladini, R., Noriega-Crespo, A., et al. 2012, A&A, 537, A113
Paradis, D., Veneziani, M., Noriega-Crespo, A., et al. 2010, A&A, 520, L8
Pilbratt, G. L., Riedinger, J. R., Passvogel, T., et al. 2010, A&A, 518, L1
Planck Collaboration 2011a, A&A, 536, A19
Planck Collaboration 2011b, A&A, 536, A21
Planck Collaboration 2011c, A&A, 536, A24
Planck Collaboration, Ade, P. A. R., Aghanim, N., et al. 2011, A&A, 536, A23
Poglitsch, A., Waelkens, C., Geis, N., et al. 2010, A&A, 518, L2
Reach, W. T., Dwek, E., Fixsen, D. J., et al. 1995, ApJ, 451, 188
Rieke, G. H., Young, E. T., Engelbracht, C. W., et al. 2004, ApJS, 154, 25
Roussel, H. 2011, PASP, submitted
Seki, J., & Yamamoto, T. 1980, Ap&SS, 72, 79
Shetty, R., Kauffmann, J., Schnee, S., & Goodman, A. A. 2009a, ApJ, 696, 676
Shetty, R., Kauffmann, J., Schnee, S., Goodman, A. A., & Ercolano, B. 2009b, ApJ, 696, 2234
Shirey, R., Soria, R., Borozdin, K., et al. 2001, A&A, 365, L195
Skibba, R. A., Engelbracht, C. W., Dale, D., et al. 2011, ApJ, 738, 89
Smith, M. W. L., Gomez, H. L., Eales, S. A., et al. 2012, ApJ, 748, 123
Smith, M. W. L., Vlahakis, C., Baes, M., et al. 2010, A&A, 518, L51
SPIRE Observer's Manual. 2011, Herschel Space Observatory, http://herschel.esac.esa.int/Docs/SPIRE/html/spire_om.html
Stark, A. A., & Binney, J. 1994, ApJ, 426, L31
Stepnik, B., Abergel, A., Bernard, J.-P., et al. 2003, A&A, 398, 551
Strong, A. W., & Mattox, J. R. 1996, A&A, 308, L21
Strong, A. W., Moskalenko, I. V., Reimer, O., Digel, S., & Diehl, R. 2004, A&A, 422, L47
Tabatabaei, F. S., & Berkhuijsen, E. M. 2010, A&A, 517, A77
Thilker, D. A., Braun, R., Walterbos, R. A. M., et al. 2004, ApJ, 601, L39
Trundle, C., Dufton, P. L., Lennon, D. J., Smartt, S. J., & Urbaneja, M. A. 2002, A&A, 395, 519
Veneziani, M., Ade, P. A. R., Bock, J. J., et al. 2010, ApJ, 713, 959
Walterbos, R. A. M., & Greenawalt, B. 1996, ApJ, 460, 696
Williams, B. F. 2003, AJ, 126, 1312
Wilson, C. D. 1995, ApJ, 448, L97
Wolfire, M. G., Hollenbach, D., & McKee, C. F. 2010, ApJ, 716, 1191
Wright, E. L., Mather, J. C., Bennett, C. L., et al. 1991, ApJ, 381, 200
Yin, J., Hou, J. L., Prantzos, N., et al. 2009, A&A, 505, 497
Ysard, N., Juvela, M., Demyk, K., et al. 2012, A&A, 542, A21
Zhu, M., Papadopoulos, P. P., Xilouris, E. M., Kuno, N., & Lisenfeld, U. 2009, ApJ, 706, 941